Seismic ground response at Lotung: Hysteretic elasto-plastic-based 3D analyses

Seismic ground response at Lotung: hysteretic elasto-plastic-based 3D analyses

A. Amorosi

Department of Structural and Geotechnical Engineering, Sapienza University of Rome, Italy (formerly Technical University of Bari, Italy)

D. Boldini*

Department of Civil, Chemical, Environmental and Materials Engineering, University of Bologna, Italy

A. di Lernia

Department of Civil, Environmental, Building Engineering and Chemistry, Technical University of Bari, Italy

Prof. Angelo Amorosi
Sapienza University of Rome
Department of Structural and Geotechnical Engineering
via Eudossiana 18, 00184 Rome, Italy
e-mail: angelo.amorosi@uniroma1.it
phone: 0039-06-44585982

Prof. Daniela Boldini
University of Bologna
Department of Civil, Chemical, Environmental and Materials Engineering
via Terracini 28, 40131 Bologna, Italy
e-mail: daniela.boldini@unibo.it
phone: 0039-051-2090233

Dr. Annamaria di Lernia
Technical University of Bari
Department of Civil, Environmental, Building Engineering and Chemistry
via Orabona 4, 70125 Bari, Italy
e-mail: annamaria.dilernia@poliba.it

* Corresponding Author

ABSTRACT

This paper presents a non-linear finite element study to back-interpret the free field seismic response recorded at the Lotung Large-Scale Seismic Test site. The study is carried out in the time domain by the Finite Element (FE) code PLAXIS 3D, considering the vertical wave propagation of both the horizontal components of motion. The non-linear soil behaviour is simulated through a constitutive model, the Hardening Soil model with Small-Strain Stiffness (*HSsmall*), capable of describing the cyclic response of the material at different strain levels. In the paper, the constitutive response of the *HSsmall* model is firstly investigated through numerical simulations of strain-controlled cyclic shear tests under single and multi-directional conditions at low strain levels. Then, it is adopted to back-analyse the recorded free field seismic response, comparing the FE numerical results to the in-situ down-hole and surface signals recorded during two earthquakes occurred on May 20th and July 17th 1986, characterized by different peak ground accelerations.

Keywords

Lotung LSST; constitutive modelling, Finite Element analysis; seismic ground response; multidirectional shear strain conditions; numerical modelling

1. Introduction

It is well-known that soils are characterised by non-linear behaviour under cyclic and dynamic shear conditions, involving the decrease in the shear stiffness modulus and the corresponding increase in material damping with increasing shear strain level [1–4]. These variations in dynamic properties can play a major role in the seismic site response, causing a change in the amplitude, duration and frequency content of the ground motion. In addition, for strong motions soil behaviour is also characterised by the accumulation of plastic strains and the build-up of excess pore water pressure: those features should also be accounted for in a realistic simulation of the wave propagation problem.

The seismic ground response analysis has traditionally been carried out by means of one-dimensional equivalent linear approaches, typically based on frequency domain numerical schemes [5–7] in which the soil is modelled as a single-phase medium. This method iteratively converges towards the solution adopting for each soil layer constant values of dynamic soil properties during the calculation step, selected as a function of the representative strain level attained in the previous iteration. Though this approach can be considered as a useful tool in the engineering practice, due to its simplicity and low computational requirements, it presents a number of shortcomings: for example, it considers a unique strain level for each soil layer as representative of the whole loading history, it does not take into account the plastic response of the material nor the volumetric-deviatoric coupling responsible of the pore water pressure variations and it should only be used to analyse those cases for which the one-dimensional assumption holds, neglecting any multi-directionality in the strain history of the real wave propagation problem.

An alternative and more realistic methodology is provided by the finite element (FE) scheme in the time-domain [8], taking into account the solid-fluid interaction by means of a coupled effective stress formulation [9,10], more complex geometrical schematisations (including 2D and 3D problems as well as the presence of more than one component in the seismic input) and the possible interaction with underground or above-ground structures. In this approach, the soil behaviour can be described using either simple (i.e. linear visco-elastic or visco-elasto-plastic models [11,12]) or more sophisticated non-linear constitutive models. In contrast to the equivalent linear method, such a numerical approach is not often adopted in the engineering practice, possibly because of the lack of adequate expertise among users and of the difficulties related to the calibration of the constitutive models, this latter limitation being especially true for more advanced constitutive laws.

In this context, it is worth identifying a compromise in terms of constitutive assumptions and calculation schemes, in order to ensure a realistic prediction of the soil behaviour at the minimum computational cost.

To this purpose, in this paper a constitutive model, named *Hardening Soil model with small strain stiffness* (*HSsmall*), is employed to numerically simulate the seismic ground response. The constitutive model, available in the library of the commercial Finite Element code PLAXIS [13], is an isotropic hardening elasto-plastic hysteretic model, based on the combination of the *Hardening Soil* model, proposed by Schanz et al.

[14], with the *Small-Strain Overlay* model suggested by Benz and co-workers [15,16]. It allows to take into account the non-linear behaviour of soil even at very small strain, introducing a pre-yield para-elastic hysteretic scheme, which controls the shear modulus degradation and the corresponding variation of the damping ratio. The calibration of the model parameters is relatively straightforward as it requires the shear stiffness and damping ratio decay curves, in addition to the shear wave velocity profile, as additional input data, together with standard soil parameters typically available in any well conducted soil characterisation.

Though the *HSsmall* model has been implemented and extensively validated for 2D and 3D static geotechnical applications (e.g. [17,18]), relatively few contributions are available in the literature for dynamic conditions [19,20].

In the present study, the *HSsmall* model is firstly validated at the element level through numerical simulations of strain-controlled cyclic shear tests, aiming at investigating the constitutive response under conventional single- and multi-directional simple shear conditions, this latter considered more representative of what occurring during real seismic events. The constitutive model is then adopted to back-analyse the seismic ground response observed at the Large-Scale Seismic Test (LSST) site in Lotung, Taiwan, with reference to the motions recorded along a down-hole array during the two earthquakes event of May 20th and July 17th 1986 (denominated LSST7 and LSST11, respectively).

The Lotung LSST experimental site has been extensively studied in the past due to its richness in terms of surface and subsurface accelerometric measurements: as such it has often been adopted as a reference to test the predictive capabilities of constitutive models and numerical codes tackling the site response problem. For example, in [21] one-dimensional site response analyses were performed under plane-strain conditions (2D), considering both horizontal components of the LSST7 seismic motion, though applied separately, adopting a hypoplastic and a visco-hypoplastic constitutive model. Furthermore, Borja and co-workers [22–24] proposed a bounding surface plasticity model formulated in terms of total stresses to numerically back-predict the LSST7 downhole motion by means of a FE soil column model. Lee and co-workers [25] evaluated both linear and non-linear soil response using strong and weak motions recorded during 13 earthquakes occurred at LSST test site, highlighting the crucial role of non-linearity on the back-prediction of high intensity earthquakes.

This paper presents a three-dimensional numerical approach to reproduce the observed free field site response, considering each horizontal component, North-South (NS) and East-West (EW), of the input motion as applied singularly or simultaneously, and modelling the soil by the elasto-plastic *HSsmall*. The FE results, in terms of accelerograms and spectra, are compared to the in-situ free field recorded down-hole and surface ones, to validate the calculation scheme and to emphasise the role of the input multi-directionality effects on the soil response. The main purpose of the study is to validate the capability of the adopted constitutive model to back-predict the seismic ground response by means of a 3D numerical approach which proves to be a useful tool to investigate both simplified (such as one-dimensional site response analyses) and possibly more complex dynamic problems (e.g. dynamic soil-structure interaction problems).

2. The case study of Lotung

Lotung, a highly seismic region in the North-East of Taiwan, was selected as the site of the LSST research project, led by Electric Power Research Institute (EPRI) in cooperation with Taiwan Power Company (TPC). The LSST program started in 1985 and consisted in studying the seismic ground response and the dynamic soil-structure interaction of two small-scale (1/4-scale and 1/12-scale models) nuclear power plant containment structures.

The LSST site was extensively instrumented to record the soil and the small-scale models response during earthquakes. The site instrumentation consisted in surface arrays installed along three arms (ARM 1, 2 and 3) of radius of about 47 m from the 1/4-scale structural model and two down-hole arrays (DHA and DHB) placed approximately 3 m and 49 m from the edge of the 1/4-scale model along ARM 1, as depicted in Fig. 1. Each down-hole array recorded the soil motion at depths of 6 m, 11 m, 17 m and 47 m by means of triaxial accelerometers oriented along NS and EW horizontal and vertical directions [26].

In this paper, the free field seismic ground response is investigated with reference to the two horizontal acceleration components (EW and NS) recorded by the DHB down-hole array during the seismic events occurred on May 20th 1986 (LLST7 event) and July 17th of the same year (LSST11 event). These earthquakes (Table 1) are characterised by different peak acceleration, shaking duration (35.48 s and 17.27 s, respectively) and frequency content bandwidth. In particular, the LSST7 event might be classified as a strong motion earthquake, characterised by low frequency content, while the LSST11 event is a weak motion characterised by high frequency content. The acceleration time histories recorded at the depth of 47 m (DHB-47 in Fig. 2), assumed herein as the bottom of the modelled soil deposit, were considered as the input ground motion for each seismic event.

The LSST site is located on the Lanyang River plain, characterised by two layers of recent alluvium and a Pleistocene deposit, overlying a Miocene basement, placed at 400 m below the ground surface [27]. The local geological profile near the 1/4-scale structural model is characterized by a layer of silty sand extended from the ground surface down to about 17 m, overlying a 6 m layer of sand with gravel. Below this layer, the soil deposit is characterised by a stratum of silty clay down to 47 m, interlayered by an inclusion of sand with gravel between 29 m and 36 m, as depicted in Fig. 3a. Groundwater level is located at the depth of about 1 m below the ground surface and the pore pressure distribution is hydrostatic.

The geotechnical characterisation of the soil deposit is based on the few available in-situ tests and on previously published back-analysed seismic data, accessible from the literature [23,24,28,29].

In particular, the strength properties of coarse-grained soils are obtained from SPT tests (Fig. 3b), using the approach proposed by De Mello [30], while typical values are assumed for the silty clay layer, as reported in Table 2. A total unit weight of 19.6 kN/m^3 is adopted as an average value for the whole soil deposit [28].

The shear wave velocity profile is obtained from cross-hole tests as summarised in Borja et al. [23], ranging from a value of about 100 m/s at ground surface to about 300 m/s at a depth of 47 m (Fig. 3c).

With reference to the upper silty sand layer (0 – 17 m), the assumed shear modulus and damping ratio decay curves are those evaluated by Zeghal et al. [29]. The Authors determined these dynamic properties at three

different depths (6 m, 11 m and 17 m from the ground surface), based on the back-interpretation of 18 earthquake signals recorded along the array between 1985 and 1986.

For the numerical simulation, the shear modulus and damping ratio curves obtained at the depth of 11 m are assumed as representative of average dynamic soil properties of the entire silty sand layer (0 m to 17 m below ground surface), as recommended in [24]. Due to the lack of specific experimental data, the shear modulus and damping ratio decay curves suggested by Vucetic & Dobry [3] for a plasticity index PI equal to 0 % and 20 % are assumed for the coarse-grained and silty soil layers, respectively (Fig. 4).

3. The soil constitutive model: *HSsmall*

3.1 Model description

The constitutive model *HSsmall* was proposed by Benz [16] as an evolution of the well-known Hardening Soil model (*HS*) [14] by including the elastic small-strain overlay model developed by Benz et al. [15].

The *HSsmall* model allows to describe the hysteretic para-elastic behaviour of soil at very small strains by introducing two additional parameters to the *HS* model formulation: the initial shear modulus G_0 and the shear strain level $\gamma_{0.7}$ at which the secant shear modulus G_s is reduced to about 70% of G_0. This latter parameter controls the shape of the modulus reduction curve, which is implemented as a modified version of the simple hyperbolic law proposed by Hardin & Drnevich [1]

$$\frac{G_s}{G_0} = \frac{1}{1 + 0.385 \frac{\gamma}{\gamma_{0.7}}} \tag{1}$$

The derivative of Eq. (1) with respect to the shear strain provides the expression of the tangent shear stiffness modulus G_t, which is bounded by a lower cut-off value corresponding to the elastic unloading-reloading shear stiffness modulus G_{ur} (Eq. (2)):

$$G_t = \frac{G_0}{\left(1 + 0.385 \cdot \frac{\gamma}{\gamma_{0.7}}\right)^2} \geq G_{ur} = \frac{E_{ur}}{2\left(1 + \nu_{ur}\right)} \tag{2}$$

When the strain level reaches the limit $\gamma_{cut\text{-}off}$

$$\gamma_{cut-off} = \frac{\gamma_{0.7}}{0.385}\left(\sqrt{\frac{G_0}{G_{ur}}} - 1\right) \tag{3}$$

the tangent shear stiffness modulus G_t becomes constant and equal to G_{ur}.

The secant shear modulus given by Eq. (1) is calculated considering a scalar strain-history dependent value γ_{Hist}:

$$\gamma_{Hist} = \sqrt{3}\frac{\left\| \underline{\dot{e}}_{km} \underline{H}^*_{ml} \right\|}{\left\| \underline{\dot{e}}_{kl} \right\|} \tag{4}$$

where $\underline{\dot{e}}_{kl}$ is the current deviatoric strain rate tensor in principal directions and $\underline{H}^*_{kl}$ is an updated strain tensor, also evaluated along the principal directions of $\dot{e}_{kl}$, that memorises the deviatoric strain history of the

material. From a geometrical prospective, the scalar shear strain indicator γ_{Hist} is a projection of the strain history onto the actual loading direction.

According to Benz [16], the updated strain history tensor $\underline{H}^*_{kl}$ is calculated as a function of a diagonal transformation tensor $\underline{T}_{km}$, which intervenes when a loading reversal is detected. Thus, starting from an initial strain state, memorised in the strain history tensor $\underline{H}_{mn}$, the updated the strain history tensor $\underline{H}^*_{kl}$ is determined according to Eq. (5):

$$\underline{H}^*_{kl} = \underline{T}_{kl}\left(\underline{H}_{mn} + \delta_{mn}\right)\underline{T}_{nl} + \dot{e}_{kl} - \delta_{kl} \tag{5}$$

where δ_{kl} is the unit second-order identity tensor. Each principal direction is checked separately for any possible reversal of loading. Whenever a loading reversal is identified, the strain tensor $\underline{H}_{kl}$ is partially or fully reset and the updated scalar γ_{Hist} is introduced in Eq. (1) as γ to define the current shear stiffness. As a consequence, the same shear stiffness modulus describes the stress-strain relationship along all loading directions in a multi-axial loading condition.

The hysteretic behaviour in unloading-reloading cycles is formulated according to the Masing's rules [31]. Under cyclic conditions, a hysteresis loop is described providing a measure of energy dissipation by means of the hysteretic damping ratio, defined as ratio of dissipated energy E_D to maximum strain energy E_S. An expression of dissipated energy and stored energy is given in Eq. (6) and Eq. (7) [19]:

$$E_D = \frac{4G_0\gamma_{0.7}}{0.385}\left(2\gamma - \frac{\gamma}{1+\frac{\gamma_{0.7}}{0.385\gamma}} - \frac{2\gamma_{0.7}}{0.385}\ln\left(1+\frac{0.385\gamma}{\gamma_{0.7}}\right)\right) \tag{6}$$

$$E_S = \frac{1}{2}G_S\gamma^2 = \frac{G_0\gamma^2}{2+2\frac{0.385\gamma}{\gamma_{0.7}}} \tag{7}$$

A basic feature of the model is the dependency of the soil stiffness on stress level, which is implemented by means of a function of the effective stress and strength parameters c' and φ':

$$G_0 = G_0^{ref}\left(\frac{c'\cdot\cos\varphi' + \sigma_3'\cdot\sin\varphi'}{c'\cdot\cos\varphi' + p^{ref}\cdot\sin\varphi'}\right)^m \tag{8}$$

The parameter G_0^{ref} is the reference initial shear modulus corresponding to the reference confining pressure p^{ref} (assumed equal to 100 kPa), m is a constant that depends on the soil type and σ_3' is the minor principal effective stress. Expressions similar to the one given in Eq. (8) are used for the secant stiffness in standard drained triaxial test (E_{50}), the unloading and reloading modulus (E_{ur}) and the tangent stiffness for primary oedometer loading condition (E_{oed}).

The *HSsmall* model is an isotropic hardening elasto-plastic model, characterized by two yield surfaces: a shear hardening yield surface and a cap yield surface, introduced to delimit the elastic region for compressive stress paths. The shear hardening yield surface is a function of the deviatoric plastic strains and it can expand up to the Mohr-Coulomb failure criterion, with a non-associated flow rule. The cap yield surface is governed by plastic volumetric strains and an associated flow rule is employed.

According to its formulation, the constitutive model provides almost null values of damping ratio at very small-strain level. In order to provide a small amount of it (typically 1-2 %), viscous damping can be introduced in the FE analysis by means of the Rayleigh formulation [32]. The damping matrix is expressed as a linear combination of the mass and stiffness matrices of the system (Eq. (9)):

$$[C] = \alpha_R [M] + \beta_R [K] \tag{9}$$

where Rayleigh coefficients α_R and β_R are frequency-dependent and are obtained through the following relationship:

$$\begin{Bmatrix} \alpha_R \\ \beta_R \end{Bmatrix} = \frac{2D^*}{\omega_m + \omega_n} \begin{Bmatrix} \omega_m \omega_n \\ 1 \end{Bmatrix} \tag{10}$$

ω_m and ω_n are the control angular frequencies over which the viscous damping is equal to or lower than the target damping ratio D^*. This formulation requires a suitable strategy of calibration for the determination of the above angular frequencies, in order to introduce the required (low) values of viscous damping in the constitutive response.

3.2 Model calibration

The calibration of the *HSsmall* model is carried out with reference to the available data; a list of model parameters employed in the numerical analysis is provided in Table 2.

The reference initial shear stiffness modulus G_0^{ref} and the parameter *m* are obtained by best fitting the shear wave velocity profile, provided by the cross-hole test, as shown in Fig. 3c. The parameter $\gamma_{0.7}$ is selected in order to obtain the best approximation of the secant shear modulus and damping ratio decay curves, as shown in Fig. 4 for the para-elastic response regime. The elastic unloading-reloading shear stiffness modulus G_{ur}^{ref} is evaluated such that the ratio G_0^{ref} / G_{ur}^{ref} results equal to 4 for the silty sand layer and to 2.5 for the other soil layers, leading to fixed values for the $\gamma_{cut\text{-}off}$ (see eq. 3).

It is worth noting that in the original reference by Brinkgreve and coworkers [33] it is assumed for the para-elastic regime a constant damping ratio for shear strain amplitudes larger than $\gamma_{cut\text{-}off}$. This appears to be incorrect, as beyond this threshold limit the tangent shear stiffness is constant and equal to G_{ur}^{ref}, while the corresponding secant one decreases asymptotically towards its minimum value. Such a stiffness response implies that at that stage the hysteresis loops become narrower for increasing strain amplitude, geometrically leading to the conclusion that the related damping ratio should accordingly decrease tending asymptotically to zero. This feature will be highlighted in detail in a following section of this paper.

The stiffness parameters E_{50}^{ref} and E_{oed}^{ref} are assumed to be three times lower the elastic unloading-reloading stiffness modulus E_{ur}^{ref}, which is related to the unloading-reloading shear stiffness modulus G_{ur}^{ref} by means of the Poisson's ratio for unloading-reloading ν_{ur}. For coarse-grained soils, this parameter is assumed equal to 0.3, according to the experimental observation by Jiang et al. [33], while it is considered equal to 0.25 for the silty soil layers.

The earth pressure at rest coefficient K_0 is estimated adopting the well-known Jâky's expression [34] for coarse-grained soils, while for fine-grained layers the modified version of the same expression for overconsolidated soils $K_0^{oc} = (1 - sin\varphi') \cdot OCR^{0.5}$ is used. For the silty sand and sand with gravel soil layers the overconsolidation ratio *OCR* is fictitiously set to 10, aiming at avoiding yielding during compressive stress paths (i.e. to exclude the activation of the cap surface included in the constitutive model, not necessary for the Lotung site deposits).

Finally the failure ratio R_f, defined as the ratio of the failure deviatoric stress and the asymptotic deviatoric stress, is assumed equal to the default value of 0.9.

The frequency-dependent Rayleigh coefficients, α_R and β_R, are evaluated according to the calibration procedure proposed by [11], for which the first Rayleigh frequency f_m is estimated as the fundamental frequency of the soil deposit, while the second Rayleigh frequency f_n is assumed equal to the frequency where the amplification function of the signal between the assumed bedrock and the surface becomes lower than one. Fig. 5 shows the amplification functions of both horizontal components (EW and NS) of the input signals, obtained through a preliminary frequency domain equivalent linear analysis carried out by the code EERA [7]. The two functions are very similar for the LSST11 weak event, while they slightly differ when evaluated with reference to the more intense LSST7 earthquake, due to the induced non-linear response. As far as the LSST7 event concerns (Fig. 5a), the control Rayleigh frequencies are identified by considering the amplification function relative to the EW component of the seismic event, characterized by a slightly lower value of the second control frequency f_n as compared to that of the NS component, in order to better fit the target value of the damping ratio D^* equal to 1% in the relevant frequency range of the event (f_m equal to 1 Hz and f_n equal to 3.5 Hz). A similar approach was adopted for the LSST11 event (Fig. 5b), leading to a first control frequency f_m equal to 1.3 Hz and a f_n of 10 Hz, roughly corresponding to the average value of the first and second crossing of the amplification factor with the value of one. The corresponding Rayleigh damping curves are plotted in the same figure with the target damping value D^*.

4. Validation of the constitutive model

4.1 Numerical model

The cyclic response of the constitutive model is validated through the simulation of strain-controlled cyclic shear tests on a weightless soil cubic volume of 0.1 m width (Fig. 6), carried out by using the 3D version of the Finite Element code PLAXIS [13]. For sake of simplicity, the numerical simulations are performed using the soil parameters relative to the upper silty-sandy layer of the Lotung site (Fig. 3a).

The soil element is subjected to either single- or multi-directional cyclic shear tests, those latter named *L-shaped*, *triangular*, *quadrangular* and *butterfly* as a function of the imposed strain paths (Fig. 7), to highlight the influence of the strain history on the mobilised shear stiffness.

The aim of these numerical tests is that of investigating and validating the cyclic para-elastic response of the model. To this purpose, prior to the application of the cyclic shearing, the soil element is preliminary

subjected to load-controlled triaxial paths, in order to enlarge the elastic domain of the material. These pre-shearing phases consist in an isotropic loading and unloading, which allow the expansion of the cap yield surface, followed by a deviatoric loading and unloading path, causing a similar enlargement of the shear hardening yield surface.

For the simulation of triaxial loading paths (Fig. 8a), boundary conditions are characterised by vertical fixities and free horizontal displacements at the bottom of the soil element; nodes on one of the two planes parallel to the *y*-*z* plane are fixed along the *x* direction and free to move along *y* and *z* axes, while on the opposite side uniform horizontal pressures are imposed; accordingly, one of the two planes parallel to the *x*-*z* plane is not allowed to move along the *y* direction and is free along *x* and *z* axes, while uniform pressures are applied on the opposite sides, as depicted in the figure. The intensities of pressure are selected to achieve the required mean effective stress and deviatoric stress values summarised in Table 3.

One-directional shear cyclic conditions are obtained by imposing uniform displacements along one horizontal direction (i.e. along the *x*-axis) at the top of the cube and triangular displacement distributions on the vertical sides parallel to *y*-*z* plane, keeping fixed the nodes along the horizontal *y*-axis and the vertical directions; the bottom of the soil element is fixed in all directions (Fig. 8b). The amplitude of displacements varies with time according to a sinusoidal signal of period equal to 10 s. Different maximum values are imposed, corresponding to shear strain levels ranging from very small (0.0001 %) to relatively large ones (0.5 %).

Under multi-directional shearing, boundary conditions consist in prescribed displacements on the top and on all the vertical sides of the soil element in both horizontal directions, as previously described, while vertical displacements are not allowed (Fig. 8c). The displacement distributions follow harmonic signals characterised by the same maximum amplitude ($\gamma = 0.05\%$) and different frequency or phase-lag, according to the selected deformative path, except for the *triangular* strain path. In fact, this latter is employed by applying linear variation of displacements with time, characterised by constant strain increment (0.0001 %).

During the *L-shaped* path (Fig. 7a) the soil element is imposed to deform in each horizontal direction separately, i.e. after the first cycle of displacements along *x*-axis, displacements are applied along the perpendicular direction (*y*-axis). Under the *triangular* path (Fig. 7b), the soil element experiences a simultaneous application of both components of deformation, until the maximum shear deformation ($\gamma = 0.025\%$) is attained along *y*-axis; after this stage, the loading direction is reversed along *y*-axis, while keeps increasing along the *x*-axis until the maximum shear strain $\gamma = 0.05\%$ is attained. The *quadrangular* strain path (Fig. 7c) makes the soil element experience a sequential application of the two components of shear strain, i.e. after the maximum shear deformation is achieved along the *x*-direction, a strain increment along the perpendicular direction (*y*-axis) is applied, keeping fixed the strain in the previous direction. Then, the same deformative path is followed in the reverse way, resulting in unloading conditions. Finally, during the *butterfly* deformation path (Fig. 7d) the soil volume element is subjected to contemporary and different strain increments in both horizontal directions, resulting in a deformation vector describing a butterfly-shaped path in the *x*-*y* plane.

A time step of 0.01 s is assumed during all the shear cyclic test simulations.

4.2 Numerical results for simple shear cyclic tests

The typical hysteretic response of the constitutive model under one-directional shear cyclic condition is shown in Fig. 9. The shear stress-strain curve τ_{zx}-γ_{zx} is characterised by an initial stiffness corresponding to the small-strain shear stiffness modulus G_0, which decreases with the strain level according to the shear modulus reduction curve, down to the minimum value corresponding to G_{ur}. Once the direction of shear strain increment is reversed, the strain history tensor $\underline{H}$ is reset and the shear stiffness regains the maximum recoverable value, determined according to Eq. (1) as a function of γ_{Hist}.

The pre-shearing triaxial loading paths leads to a fully reversible response for cycles characterised by maximum shear strain lower than 0.1%. This is confirmed by the fact that, in these cases, the stress-strain curve upon unloading passes through the origin of the axes. At higher strain levels (i.e. γ = 0.2 % in Fig. 9), the material behaviour is characterised by the accumulation of plastic deformation, due to the engagement of the shear hardening yield surface; associated to this is the increase of energy dissipation. At very high strain level, the shear hardening yield surface enlarges up to the Mohr-Coulomb failure criterion, thus perfectly plastic response occurs.

The secant shear stiffness and the relative damping ratio are evaluated for each cycle and compared to the analytical curves at the base of the constitutive formulation (e.g.: equations 1, 6 and 7), as shown in Fig. 10. The damping ratio is estimated as the ratio between the area included within the hysteresis loop in the shear stress-strain plane and the corresponding triangular area subtended by the secant to the first loading portion of the hysteresis loop for the same cycle. A good agreement between the analytical curves and the calculated ones is observed at different strain levels, until the cut-off deformation is reached. In fact, once this strain level is exceeded, the secant shear stiffness shows larger values than those provided by the reference curve, while the damping ratio undergoes a reduction, for a maximum shear strain γ equal to 0.1%, followed by a sudden increase once the deviatoric yield surface is engaged. The decrease in the damping ratio should be related to the fact that the *HSsmall* model assumes, in its para-elastic formulation, a constant value of the tangent stiffness modulus when the cut-off strain level is overtaken. Thus, the increment in stored energy as calculated by the stress-strain curve is larger than the increment of the corresponding dissipated energy. When the plastic response becomes predominant (i.e. γ > 0.2 %), the associated damping ratio increases, being no longer uniquely associated to a para-elastic formulation, but rather strongly dependent on the irreversible response of the model.

4.3 Numerical results for multi-directional shear cyclic tests

The para-elastic cyclic response of the *HSsmall* model under multi-directional shear conditions is shown in Fig. 11, in terms of stress-strain curves τ_{zx}-γ_{zx} and τ_{zy}-γ_{zy} . The single shear test numerical simulations (indicated as “one-directional path”) are also shown for comparison.

With reference to the *L-shaped* strain path, a perfect correspondence is observed between the stress-strain curves τ_{zx}-γ_{zx} and τ_{zy}-γ_{zy} as obtained in one-directional and multi-directional tests (Fig. 11a and b). This response should be related to the particular strain path imposed: in fact, the first loading and unloading stage along the *x* direction ends up not influencing at all the subsequent cycle along the perpendicular direction, as the strain history tensor $\underline{H}$ is brought back to its reset configuration at the end of the first closed loop, causing the complete recover of the initial shear stiffness modulus. As such, the model exhibits a constitutive response identical along both planes of shearing.

Along the *triangular* strain path (Fig. 11c and d), the soil element is subjected to a first stage in which both strain components γ_{zx} and γ_{zy} increase up to 0.025 %, followed by a second one in which γ_{zy} decreases down to zero, while γ_{zx} keeps increasing up to 0.05 %. The coexistence of both components of deformation has a direct impact on the response of the model, which exhibits a softer behaviour as compared to that experienced under one-directional conditions. The first loading stage is characterised by the same stress-strain curve on both τ_{zx}-γ_{zx} and τ_{zy}-γ_{zy} planes, due to the fact that a unique tangent stiffness modulus is associated to each loading direction, determined as a function of the scalar value γ_{Hist}. When the loading reversal is detected along *y* direction, the strain tensor $\underline{H}$ is partly reset and the tangent stiffness modulus regains the maximum recoverable value, which is lower than the initial one G_0 (G_t is about 82% of G_0). The reversal of the strain increment direction γ_{zy} affects the shear stress-strain curve τ_{zx}-γ_{zx}, which shows a sharp change in its slope. During the following stage, the stress-strain curves along each direction is characterised by the same mobilised tangent stiffness.

The *quadrangular* strain path leads to the curves shown in Fig. 11e and f. In the first stage purely γ_{zx} strain increments are applied (up to a maximum shear strain equal to 0.05 %), thus the resulting stress-strain curve is equivalent to that obtained under the standard one-directional strain path (Fig. 11a). At the subsequent application of displacement along the *y*-direction, which produces a sharp variation of the strain increment direction, the corresponding stress-strain curve τ_{zy}-γ_{zy} is characterised by a lower stiffness as compared to what resulting from the first portion of the test. This response is related to the coexistence of both components of deformations, which affects the value of the scalar shear strain γ_{Hist}. In particular, the variation of the strain increment direction induced by the application of the shearing along *y* implies a reset of the strain tensor $\underline{H}$, which keeps being affected by the previously experienced shear strain history along the *x*-direction. As a consequence, the mobilised tangent shear stiffness modulus G_t assumes a lower value as compared to its maximum (G_t reduced to about 86% of G_0). During the following unloading phase along the *x*-direction, the stress-strain relationship τ_{zx}-γ_{zx} is still influenced by the coexistence of both components of deformation and the response is less stiff as compared to the single-directional one. Finally, the last unloading stage of the shear test is imposed along the *y*-direction and characterised by a shear stress-strain curve τ_{zy}-γ_{zy} identical to the one obtained under one-directional strain conditions (i.e. γ_{zx} is back to zero and the tangent shear stiffness modulus is fully regained), but slightly shifted due to the different maximum shear stress experienced.

During the more complex *butterfly* strain path, which is characterised by a larger strain amplitude, the soil element is subjected to concurrent shear strain increments characterised by different intensities along each horizontal direction (Fig. 12). During the primary loading the backbone curve τ_{zy}-γ_{zy} shows an apparent stiffer behaviour as compared to that exhibited by the corresponding τ_{zx}-γ_{zx} curve. This particular response indicates that, at a generic time step, the selected tangent shear stiffness, estimated as a function of the scalar shear strain γ_{Hist}, is the same along both directions and is governed by the largest shear strain γ_{zy}, which increases more rapidly during the initial portion of the test. Once the first strain increment reversal occurs, along the *y*-direction after t = 1.25 s, the strain tensor $\underline{H}$ is reset and the tangent stiffness regains a larger value: this feature not only affects the related τ_{zy}-γ_{zy} stress-strain relationship along the *y*-direction, but also that predicted in the other direction τ_{zx}-γ_{zx}. It follows that this latter curve is characterised by a sharp change in its slope due to the above discussed sudden increase in stiffness. An analogous response is detected during the subsequent stages of shear test simulation. The stress-strain curves end up being described by hysteresis loops enclosing smaller areas, thus characterised by the mobilisation of a smaller amount of damping as compared to what expected under single-directional shear tests.

The above numerical results indicate that the para-elastic constitutive response under cyclic multi-directional conditions can be characterised by an overall softer and less dissipative behaviour as compared to that obtained under more conventional one-directional response, for strain amplitudes larger than the reference $\gamma_{cut\text{-}off}$. This unrealistic feature is partly compensated by the plastic-strain induced dissipation that is activated for about the same strain level.

As a matter of fact, no experimental results are available to qualitatively confirm or falsify the numerical evidences discussed above with reference to multi-directional cyclic small strain behaviour of soils, as the only laboratory results discussed in the literature refer to much larger cyclic strain amplitude, well out of the range considered in this paper (e.g. [35–39]).

5. Seismic ground response analyses for the Lotung case study

5.1 Numerical model

The back-predictions of the free-field ground response observed at the Lotung site are performed in the time domain, applying the two horizontal components of the DHB-47 acceleration time history recorded during the LSST7 and LSST11 earthquakes, both separately and simultaneously. The acceleration time histories obtained by the two non-linear analyses are compared to the motions recorded at ground surface (FA1-5) and along the downhole array DHB at depths of 6 m (DHB-6), 11 m (DHB-11) and 17 m (DHB-17) (Fig. 1). The geometrical model adopted in the finite element analyses consists of a soil column characterised by a width of 10 m x 10 m and a height equal to that of the investigated soil deposit, e.g. 47 m. The soil domain is discretised with 5329 10-noded tetrahedral elements. In the vertical direction the deposit is divided into 47 layers of unit thickness, in order to ensure the elements' size to be smaller than one-eighth of the wavelength

associated with the maximum frequency component f_{max} of the input signals. To this purpose, the LSST11 event was filtered in order to cut off frequencies higher than 20 Hz.

The boundary conditions adopted in the static stage are the customary ones: total fixities are imposed to the nodes at the bottom of the mesh, while nodes on the lateral sides of the model are not allowed to move in both horizontal directions. During the dynamic stages, *tied nodes* boundary conditions are assumed, consisting in connecting nodes on corresponding vertical sides to force them having the same horizontal displacements, while vertical displacements are set equal to zero. This condition is achieved by manually introducing horizontal node-to-node anchor elements, characterised by a very high value of axial stiffness EA, equal to 10^9 kN. In order to avoid any modification of the horizontal stress conditions in the soil domain when switching from the static boundary conditions to the dynamic ones, pressures corresponding to the lithostatic distribution of horizontal effective stresses were introduced along the vertical surfaces of the model. This precaution is particularly important when a stress-dependent constitutive model, as the one employed here, is adopted.

All dynamic analyses were carried out under the assumption of fully undrained conditions.

The Generalized Newmark method is employed as time integration scheme during the dynamic stages, with Newmark parameters $\beta_1 = 0.6$ and $\beta_2 = 0.605$. These values ensure the algorithm to be unconditionally stable, while being dissipative only at high frequencies [9,11]. A time step dt of 0.005 s was adopted, largely fulfilling the required constraints suggested by Bathe [40].

5.2 Seismic ground response

The numerical results of the wave propagation analyses performed applying a single-direction input signal, i.e. considering separately the EW and NS components of the acceleration time histories, are shown in Figs. 13 – 16, with reference to both seismic events LSST11 and LSST7. In detail, the figures show the acceleration time histories and Fourier spectra at the ground surface and at a depth of 11 m and 17 m (denoted respectively with the labels FA1-5, DHB-11 and DHB-17). In the same figures the ground motion recorded in-situ along the downhole array DHB at the same depths is also plotted for comparison.

Results obtained for the weaker LSST11 input signal are depicted in Figs. 13 and 14. It appears that the computed response at different depths is similar to the corresponding recorded one, particularly for the NS component, confirming the correctness of the shear wave velocity profile assumed in the model. Nevertheless, it might be identified a general tendency to overestimate the amplitude of motion, due to the low damping involved during the wave propagation process. This should be ascribed to the small average strain level induced during the weak seismic motion, of about 0.01 %, which leads to an overall underestimation of the actual damping ratio as compared to the experimental one, in spite of the added 1% Rayleigh-based viscous damping. This is particularly true for the EW component, which is characterised by a lower peak ground acceleration than the NS one. Such a feature can be further highlighted by comparing the results of the FE analyses with the corresponding ones obtained by a standard equivalent linear approach. At the scope, Fig. 14a and d also shows the Fourier spectra for the EW and NS components at the ground surface as obtained by two analyses carried out by the code EERA. It clearly indicates that a similar response

is obtained performing the linear equivalent and the FE analyses, the major difference between the two being the peak amplitudes of the spectra, which are larger in the FE analyses.

With reference to the more intense event LSST7 (Figs. 15 and 16), the numerical simulations are in fair agreement with the recorded data, especially for the EW component, both in terms of acceleration time histories and Fourier spectra. A slight over-prediction of the peak acceleration can be detected at ground surface and at a depth of 11 m. The NS component event also leads to numerical results comparable with the observed response, with a slight under-prediction of the peak acceleration at the ground surface. Zero crossings of both acceleration time histories are well predicted by the numerical analyses, those latter showing a good fit with measured data also in terms of Fourier spectra.

When both horizontal components of the LSST11 input signal are simultaneously applied, the comparison between numerical and in-situ data is still satisfactory, though peak accelerations are slightly overestimated with respect to the measured values, as depicted in Figs. 17 and 18. It is worth highlighting the influence of the coexistence of both components on the soil response along each direction: in fact, the predicted Fourier spectra along the NS direction show at each depth an over-prediction of the spectral amplitude in the frequency range 7-15 Hz.

The predicted response under multi-directional input motion is comparable to that obtained under single-directional condition in terms of mobilised secant shear stiffness, as identified by the stress-strain curves shown in Fig. 19a and b. The induced strain level during LSST11 is relatively small (i.e. in the order of about 0.01 %).

A similar pattern is also observed when the strong motion event LSST7 is applied to the model. In fact, Figs. 20 and 21 show the tendency of the numerical model to slightly over-predict the observed ground response when both horizontal acceleration time histories are considered. The predicted Fourier spectra indicate that the model is capable of reproducing the overall frequency content of the signals as observed at different depths, though showing a systematic over-prediction of the amplitude around 0.85 Hz.

This behaviour is likely to be related to the tendency of the model to predict a reduced amount of hysteretic damping under multi-directional excitation, especially when relatively large strain levels are attained during the seismic analyses (e.g. the maximum induced strain level is in the order of 0.3 %). This is illustrated in Fig. 22a and b, where the stress-strain curves as obtained at a depth of 11 m during the analyses of the weak and strong events are compared: multi-directional conditions lead to thinner - thus less dissipative - loops, consistently with what discussed in section 4.3. As a side effect of the above behaviour, a more significant numerical noise was generated at high frequencies during the multi-directional seismic analyses. This pattern was minimised in the representation of the results by adopting a low pass filter, characterised by a cut-off frequency of 5 Hz, which was then applied to all the numerical output signals shown in Figs. 20 and 21.

In Fig. 23a and b the profile of the maximum acceleration with depth is depicted for both earthquakes along each horizontal component: a more accurate reproduction of the measured data is observed when input motions are applied singularly, consistently with the general tendency to slightly over-predict the response under multi-directional conditions.

6. Conclusions

In this paper a non-linear finite element model is employed for investigating the free field seismic ground response recorded at Lotung Large-Scale Seismic Test site along a down-hole array during the LSST7 earthquake of May 20th 1986 and the LSST11 event of July 17th of the same year. The adopted commercial FE code was selected as it allows the multi-directionality of the seismic motion to be accounted for under 3D conditions. The non-linear behaviour of soil is represented by the constitutive model Hardening Soil with Small Strain Stiffness (*HSsmall*). This latter belongs to the class of isotropic hardening elasto-plastic models and accounts for pre-yield small strain non-linear behaviour by a para-elastic formulation inspired by Masing's rules. The calibration of the *HSsmall* model parameters is relatively straightforward as only requires a few additional experimental data as compared to the usual static ones, such as a shear wave velocity profile and decay curves of shear stiffness modulus and damping ratio.

To the purpose of validating the constitutive model, strain controlled cyclic shear tests were simulated aiming at investigating the different aspects of the constitutive response under standard simple shearing conditions and multi-directional ones, with particular reference to low to medium strain levels, i.e. those relevant in most seismic site response problems.

With reference to the simple shear condition, the *HSsmall* model is capable of reproducing the expected response in terms of shear stiffness and damping ratio evolution with shear strain level. This certainly holds for the elastic (i.e. small strain) deformation regime, but also takes advantage of the engagement of the yield surface and the related accumulation of plastic strain occurring for larger cycle amplitude. This last occurrence leads to a realistic prediction of the damping at relatively large strain level. The above features do not include the capability of the model to satisfactory predict large excess pore water pressure build up and related cyclic mobility, which would require a far more articulated formulation.

A specific focus was devoted to the performance of the model under multi-directional cyclic conditions at small strain level. This because the model was meant to be used under such conditions to back-analyse the Lotung case history under 3D conditions. It emerged that the concurrent application of shear deformation along different directions influences the material response both in terms of stiffness and energy dissipation, due to the formulation of the model which somehow combines, in the small strain para-elastic regime, the response along different directions to define a unique scalar equivalent shear strain assumed as a reference to determine the instantaneous and unique (for any direction) stiffness and damping of the material. This latter relationship is obviously based on standard (single-directional) tests, such as simple shear or resonant column ones. In particular, a generally less rigid and less dissipative behaviour is observed under the investigated multi-direction shear strain paths. This numerical observations cannot be validated due to the lack of experimental data for such specific loading conditions.

Finally, the results of numerical site response analyses, performed with reference to the Lotung case study, prove to be in good agreement with the free field measurements recorded at the ground surface and at different depths, both in terms of peak acceleration and zero crossing prediction, especially when a single input motion is considered. The contemporary application of the two horizontal components produces a

slight overestimation of peak ground accelerations, to be associated to the less dissipative response of the constitutive model under such conditions, as well as some high frequencies' noise, this latter more pronounced for the strong intensity earthquake.

In general, the use of the *HSsmall* constitutive model for seismic ground response analyses can be considered affordable and valuable, provided no liquefaction/cyclic mobility features are to be included in the analysis. This study has also highlighted the need for further experimental investigations to be carried out to shed some light on the so far "grey area" of the real soils' small strain cyclic behaviour under multi-directional conditions.

References

[1] Hardin BO, Drnevich VP. Shear Modulus and Damping in Soils. J Soil Mech Found Div 1972;98:667–92.

[2] Seed HB, Idriss IM. Soil Moduli and Damping Factors for Dynamic Response Analyses. Berkeley: 1970.

[3] Vucetic M, Dobry R. Effect of Soil Plasticity on Cyclic Response. J Geotech Eng 1991;117:89–107.

[4] Darendeli MB. Development of a new family of normalized modulus reduction and material damping curves. University of Texas at Austin, 2001.

[5] Schnabel PB, Lysmer J, Seed HB. SHAKE: a computer program for earthquake response analysis of horizontally layerd sites. Report EERC 72-12. Berkley: 1972.

[6] Idriss IM, Sun JI. SHAKE91: A computer program for conducting equivalent linear seismic response analyses of horizontally layered soil deposits. Davis: 1992.

[7] Bardet JP, Ichii K, Lin CH. EERA: A computer program for equivalent-linear earthquake site response analyses of layered soil deposits. 2000.

[8] Kramer S. Geotechnical earthquake engineering. Upper Saddle River, N.J.: Prentice Hall; 1996.

[9] Zienkiewicz OC, Chan AHC, Pastor M, Schrefler BA, Shiomi T. Computational geomechanics with special reference to earthquake engineering. John Wiley; 1999.

[10] Potts D, Zdravkovic L. Finite element analysis in geotechnical engineering : theory. London: Thomas Telford; 1999.

[11] Amorosi A, Boldini D, Elia G. Parametric study on seismic ground response by finite element modelling. Comput Geotech 2010;37:515–28.

[12] Amorosi A, Boldini D. Numerical modelling of the transverse dynamic behaviour of circular tunnels in clayey soils. Soil Dyn Earthq Eng 2009;29:1059–72.

[13] Brinkgreve RBJ, Engin E, Swolfs WM. Plaxis 3D. Reference manual. 2013.

[14] Schanz T, Vermeer PA, Bonnier PG. The hardening soil model: formulation and verification. Beyond 2000 Comput Geotech 1999:281–96.

[15] Benz T, Vermeer PA, Schwab R. A small-strain overlay model. Int J Numer Anal Methods Geomech 2009;33:25–44.

[16] Benz T. Small-Strain Stiffness of Soils and its numerical consequences. University of Stuttgart, Germany, 2006.

[17] Brinkgreve R, Bakker K, Bonnier P. The relevance of small-strain soil stiffness in numerical simulation of excavation and tunnelling projects. In: HF Schweiger, editor. Numer. Methods Geotech. Eng., London: Taylor & Francis Group; 2006, p. 133–9.

[18] Fargnoli V, Gragnano CG, Boldini D, Amorosi A. 3D numerical modelling of soil-structure interaction during EPB tunnelling. Geotechnique 2015;65:23–37.

[19] Brinkgreve RBJ, Kappert MH, Bonnier PG. Hysteretic damping in a small-strain stiffness model. Proc. 10th Int. Symp. Numer. Model. Geomech. NUMOG 10 - Numer. Model. Geomech. NUMOG 10, 2007, p. 737–42.

[20] Amorosi A, Boldini D, Falcone G. Numerical prediction of tunnel performance during centrifuge dynamic tests. Acta Geotech 2014;9:581–96.

[21] Reyes DK, Rodriguez-Marek A, Lizcano A. A hypoplastic model for site response analysis. Soil Dyn Earthq Eng 2009;29:173–84.

[22] Borja RI, Smith HA, Wu WH, Amies AP. A methodology for nonlinear soil-structure interaction effects using time-domain analysis techniques. Report No 101. 1992.

[23] Borja RI, Chao HY, Montáns FJ, Lin CH. Nonlinear ground response at Lotung LSST site. J Geotech Geoenvironmental Eng 1999;125:187–97.

[24] Borja RI, Lin C-H, Sama KM, Masada GM. Modelling non-linear ground response of non-liquefiable soils. Earthq Eng Struct Dyn 2000;29:63–83.

[25] Lee C-P, Tsai Y-B, Wen K-L. Analysis of nonlinear site response using the LSST downhole accelerometer array data. Soil Dyn Earthq Eng 2006;26:435–60.

[26] Tang HT. Large-scale soil-structure interaction. Report No. NP-5513-SR. Palo Alto, California: EPRI; 1987.

[27] Anderson DG. Geotechnical synthesis for the Lotung large-scale seismic experiment. Technical Report No. 102362. Palo Alto, California: 1993.

[28] Elgamal A-W, Zeghal M, Tang HT, Stepp JC. Lotung Downhole Array. I: Evaluation of Site Dynamic Properties. J Geotech Eng 1995;121:350–62.

[29] Zeghal M, Elgamal A-W, Tang HT, Stepp JC. Lotung Downhole Array. II: Evaluation of Soil Nonlinear Properties. J Geotech Eng 1995;121:363–78.

[30] De Mello VFB. The Standard Penetration Test, State Of the Art Report. IV Panam. Conf. Soil Mech. Found. Eng., San Juan, Puerto Rico: 1971.

[31] Masing G. Eigenspannungen und Verfertigung bim Messing. Proc. 2nd Int. Congr. Appl. Mech., Zurich: 1926.

[32] Rayleigh J. The theory of sound. New York: Dover; 1945.

[33] Jiang G-L, Tatsuoka F, Koseki J, Flora A. Inherent and stress-state-induced anisotropy in very small strain stiffness of a sandy gravel. Géotechnique 1997;47:509–21. doi:10.1680/geot.1997.47.3.509.

[34] Jâky J. The coefficient of earth pressure at rest. J Soc Hungarian Archit Eng 1944:355–8.

[35] Ishihara K, Nagase H. Multi-directional irregular loading tests on sand. Soil Dyn Earthq Eng 1988;7:201–12. doi:10.1016/S0267-7261(88)80004-6.

[36] Ohara S, Matsuda H. Study on the settlement of saturated clay layer induced by cyclic shear. Soils Found 1988;28:103–13.

[37] Biscontin G. Modeling the Dynamic Behavior of Lightly Overconsolidated Soil Deposits on Submerged Slopes. 2001.

[38] Kammerer AM, Pestana JM, Seed RB. Behavior of Monterey 0/30 sand under multidirectional loading conditions. Geotech. Spec. Publ., 2005, p. 154–73.

[39] Matsuda H, Nhan TT, Nakahara K, Thien DQ, Tuyen TH. Post-cyclic recompression characteristics of a clay subjected to undrained uni-directional and multi-directional cyclic shears. NCEE 2014 - 10th U.S. Natl. Conf. Earthq. Eng. Front. Earthq. Eng., 2014.

Figure captions

Fig. 1. Location of instrumentation of the Lotung experiment site: (a) down-hole instrument arrays (b) surface instrument arrays (after Tang H.T. [26])

Fig. 2. Acceleration time histories and relative Fourier spectra recorded at DHB-47 during (a, b) LSST7 and (c, d) LSST11 earthquakes and assumed as input signal at the base of the numerical model (at z = 47 m).

Fig. 3. Local soil profile at Lotung LSST site: (a) soil stratigraphy; (b) SPT Log; (c) shear wave velocity profile from cross-hole test.

Fig. 4. Normalised tangent (G_t/G_o) and secant (G_s/G_o) shear modulus reduction curves and variation of damping ratio with cyclic shear strain assumed for different soil layer: (a) silty sand (0 – 17 m); (b) sand with gravel (17 – 23 m and 29 – 36 m); (c) silty clay (23 – 29 m and 36 – 47 m).

Fig. 5. Calibration of Rayleigh viscous damping parameters for (a) LSST7 and (b) LSST11 events, according to Amorosi et al. [11]

Fig. 6. Representation of soil volume element used for strain-controlled cyclic shear test simulation.

Fig. 7. Multi-directional shear strain paths: (a) *L-shaped* path, (b) *Triangular* path, (c) *Quadrangular* path, (d) *Butterfly* path.

Fig. 8. Boundary conditions applied on soil volume element: (a) isotropic and deviatoric loading and unloading phase; (b) shearing phase under one-directional shear test; (c) shearing phase under multi-directional shear test.

Fig. 9. Shear stress-strain curves obtained by one-directional cyclic shear test at maximum strain level of 0.05 %, 0.1 % and 0.2 %.

Fig. 10. Comparison of secant stiffness modulus reduction and damping ratio curves obtained by the model formulation and by the numerical simulation of one-directional cyclic shear tests.

Fig. 11. Shear stress-strain curves obtained by multi-directional shear test under (a, b) *L-shaped*, (c, d) *Triangular*, (e, f) *Quadrangular* and (g, h) *Butterfly* d paths, compared to those obtained by one-directional shear test.

Fig. 12. Variation of shear strain in time domain applied to *Butterfly* path shear test.

Fig. 13. Comparison between predicted and recorded response, in terms of acceleration time history, at depth of 0 m, 11 m and 17 m during LSST11 event: (a, b, c) EW and (d, e, f) NS components obtained by a single-directional analysis (singularly).

Fig. 14. Comparison between predicted and recorded response, in terms of Fourier spectra, at depth of 0 m, 11 m and 17 m during LSST11 event: (a, b, c) EW and (d, e, f) NS components obtained by a single-directional analysis (singularly). Figure 14a and d also shows the Fourier spectra for the EW and NS components at the ground surface as obtained by two analyses carried out by the code EERA.

Fig. 15. Comparison between predicted and recorded response, in terms of acceleration time history, at depth of 0 m, 11 m and 17 m during LSST7 event: (a, b, c) EW and (d, e, f) NS components obtained by a single-directional analysis (singularly).

Fig. 16. Comparison between predicted and recorded response, in terms of Fourier spectra, at depth of 0 m, 11 m and 17 m during LSST7 event: (a, b, c) EW and (d, e, f) NS components obtained by a single-directional analysis (singularly).

Fig. 17. Comparison between predicted and recorded response, in terms of acceleration time history, at depth of 0 m, 11 m and 17 m during LSST11 event: (a, b, c) EW and (d, e, f) NS components obtained by a multi-directional analysis (simultaneously).

Fig. 18. Comparison between predicted and recorded response, in terms of Fourier spectra, at depth of 0 m, 11 m and 17 m during LSST11 event: (a, b, c) EW and (d, e, f) NS components obtained by a multi-directional analysis (simultaneously).

Fig. 19. Shear stress-strain curves at a depth of 11 m from ground surface, obtained by applying singularly and simultaneously EW (a) and NS (b) horizontal components of acceleration of LSST11 event.

Fig. 20. Comparison between predicted and recorded response, in terms of acceleration time history, at depth of 0 m, 11 m and 17 m during LSST7 event: (a, b, c) EW and (d, e, f) NS components obtained by a multi-directional analysis (simultaneously).

Fig. 21. Comparison between predicted and recorded response, in terms of Fourier spectra, at depth of 0 m, 11 m and 17 m during LSST7 event: (a, b, c) EW and (d, e, f) NS components obtained by a multi-directional analysis (simultaneously).

Fig. 22. Shear stress-strain curves at a depth of 11 m from ground surface, obtained by applying singularly and simultaneously EW (a) and NS (b) horizontal components of acceleration of LSST7 event.

Fig. 23. Profile of maximum acceleration with depth obtained under single-directional (singularly) and multi-directional (simultaneously) analyses and compared to in-situ recorded data: (a) LSST7 and (b) LSST11 seismic events.

Tables captions

Table 1. Characteristics of the LSST11 and LSST7 events, occurred at Lotung, Taiwan [28].

Table 2. Material properties of the soil at Lotung site and *HSsmall* model parameters used in FE analyses.

Table 3. Stress path applied during the pre-loading triaxial phases before cyclic shear tests.

Table 1.

Event	Date	Magnitude (M_l)	Epicentral distance (km)	Peak Acceleration		
				EW (g)	NS (g)	V (g)
LSST7	20 May 1986	6.5	66.2	0.16	0.21	0.04
LSST11	17 July 1986	5	6.0	0.07	0.10	0.04

Table 2.

Parameters	Silty sand 0-17m	Sand with gravel 17-23m	Silty clay 23-29m	Sand with gravel 29-36m	Silty clay 36-47m
c' (kPa)	0	0	10	0	10
φ' (°)	30	35	24	37	24
OCR	10	10	5	10	5
K_0^{nc}	0.5	0.4264	0.5933	0.3982	0.5933
K_0^{oc}	-	-	1.327	-	1.327
G_0^{ref} (MPa)	90	115	65	160	65
$\gamma_{0.7}$ (%)	0.011	0.01	0.025	0.011	0.025
m	0.54	0	0.42	0	0.42
ν_{ur}	0.3	0.3	0.25	0.3	0.25
E_{ur}^{ref} (MPa)	60	119.5	65	164.5	65
E_{50}^{ref} (MPa)	20	39.83	21.67	54.81	21.67

Table 3

	Isotropic Loading	Isotropic Unloading	Deviatoric Loading	Deviatoric Unloading
p' (kPa)	150	100	133	100
q (kPa)	0	0	100	0

Figure 1
Click here to download Figure: Figure 1.pdf

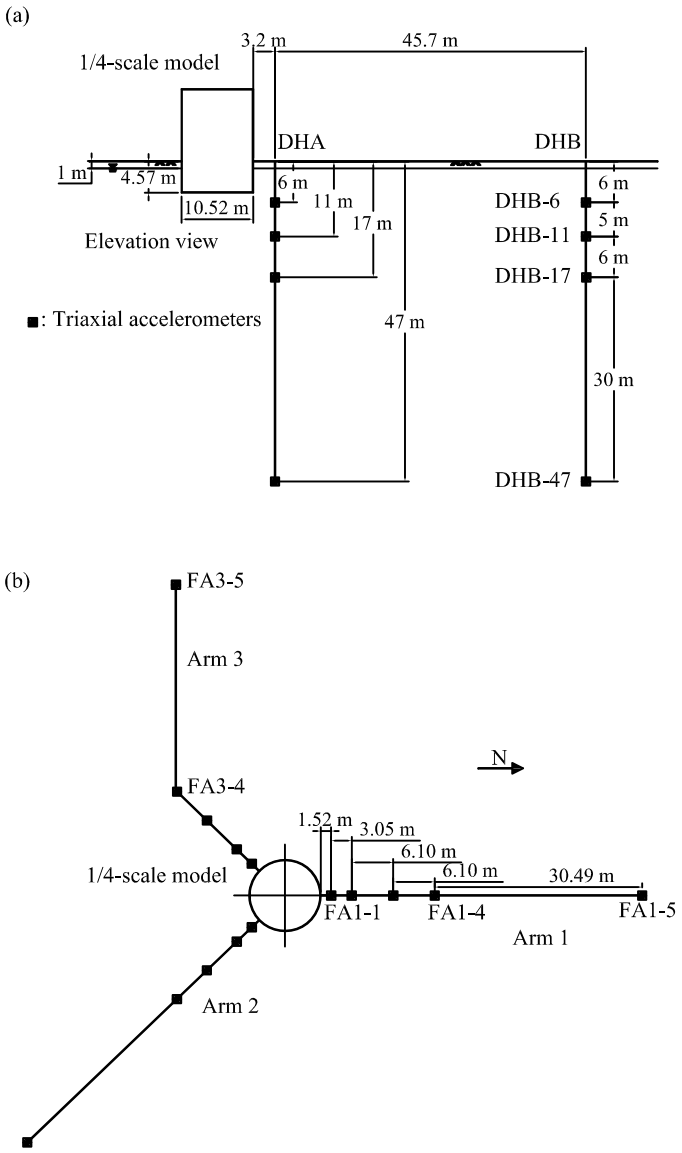

Figure 2
Click here to download Figure: Figure 2.pdf

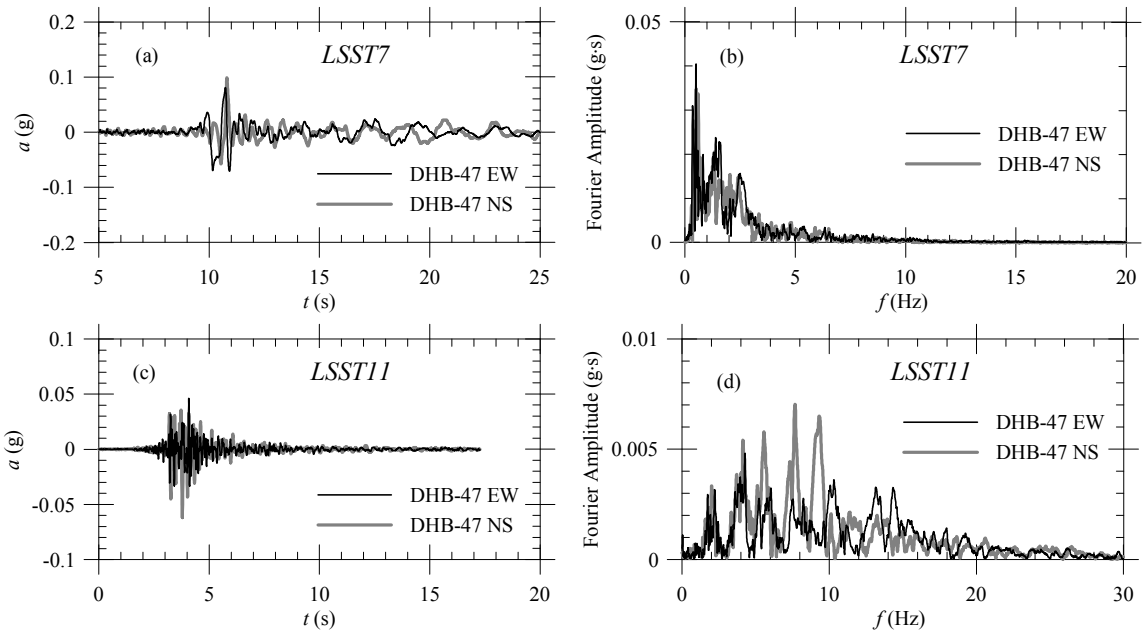

Figure 3
Click here to download Figure: Figure 3.pdf

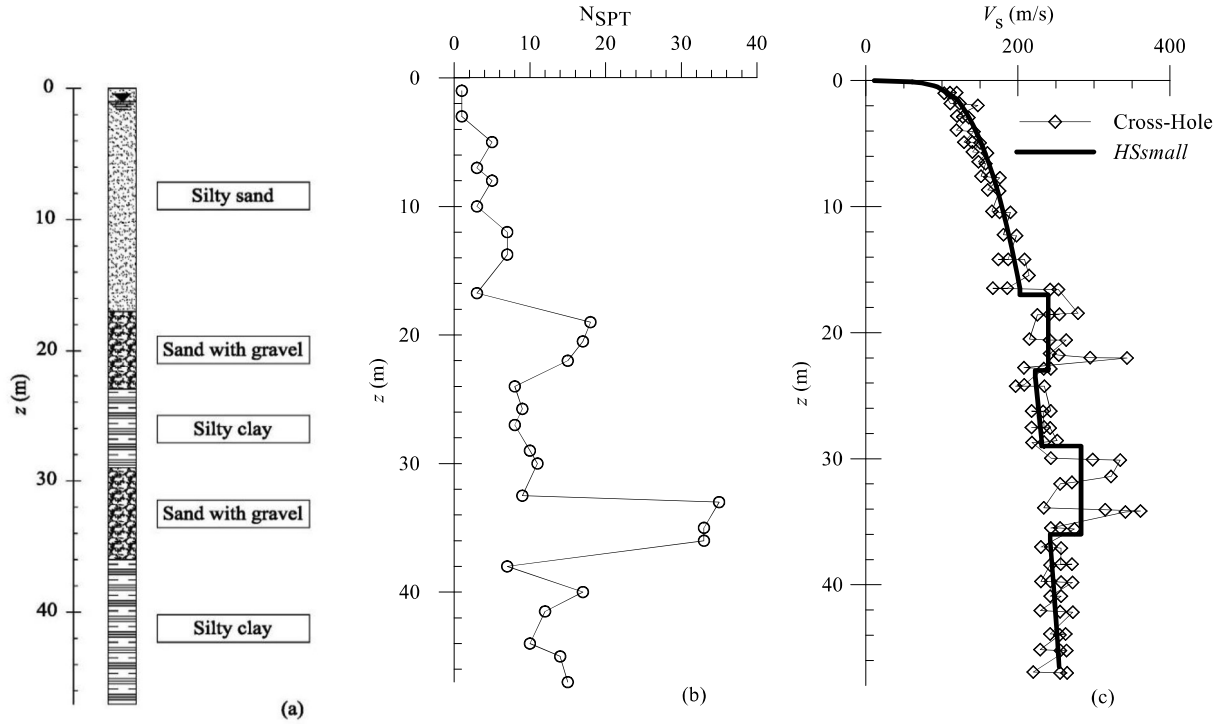

Figure 4
Click here to download Figure: Figure 4.pdf

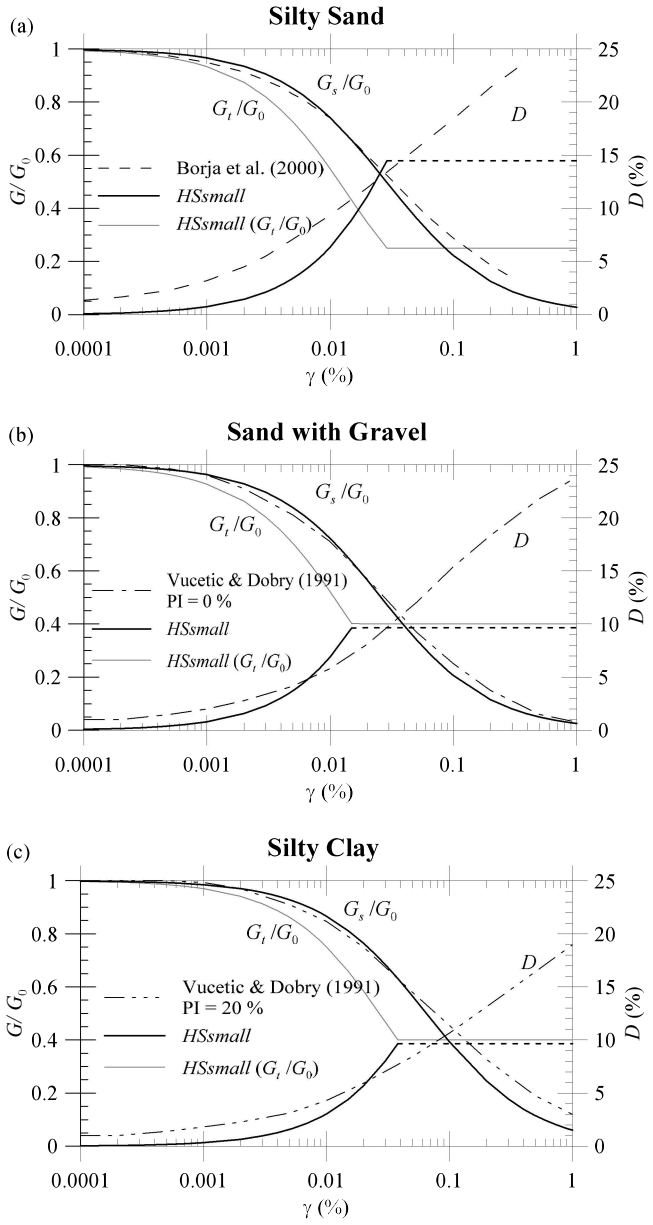

Figure 5
Click here to download Figure: Figure 5.pdf

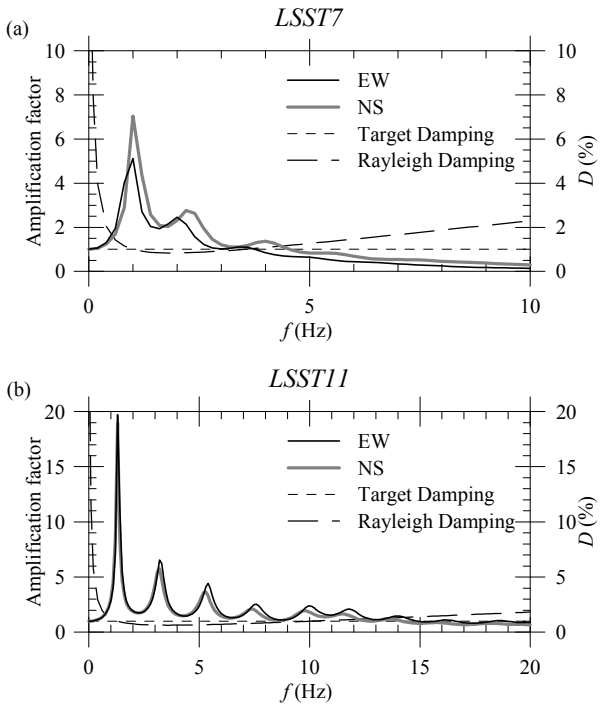

Figure 6
Click here to download Figure: Figure 6.pdf

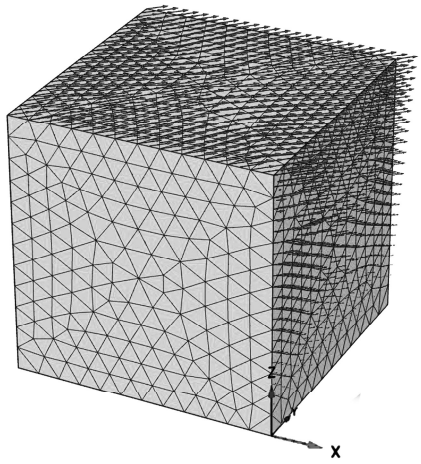

Figure 7
Click here to download Figure: Figure 7.pdf

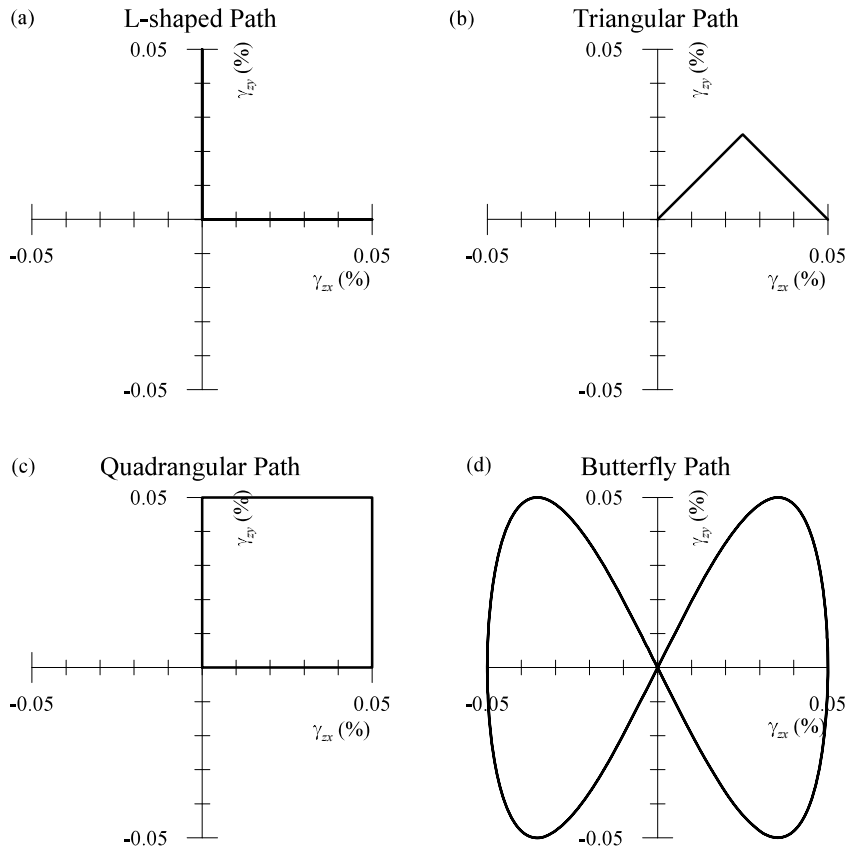

Figure 8
Click here to download Figure: Figure 8.pdf

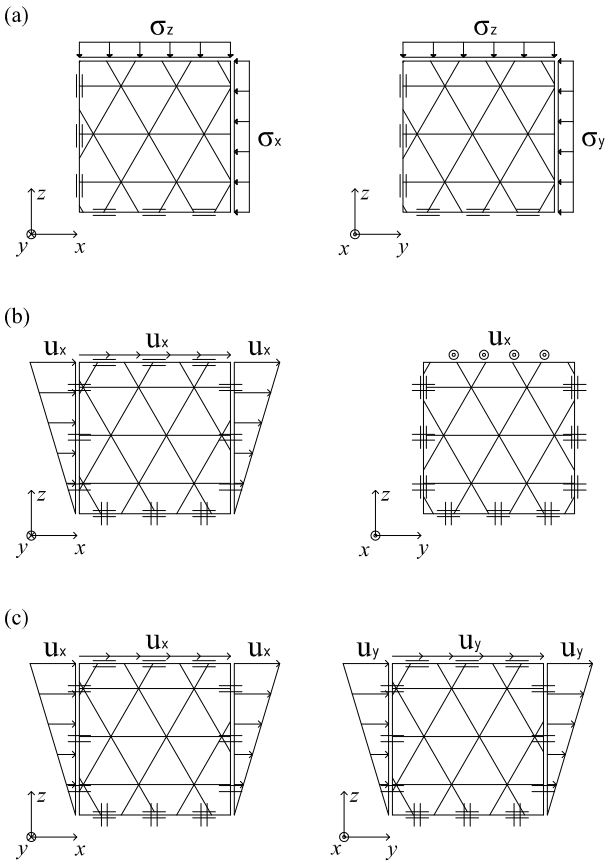

Figure 9
Click here to download Figure: Figure 9.pdf

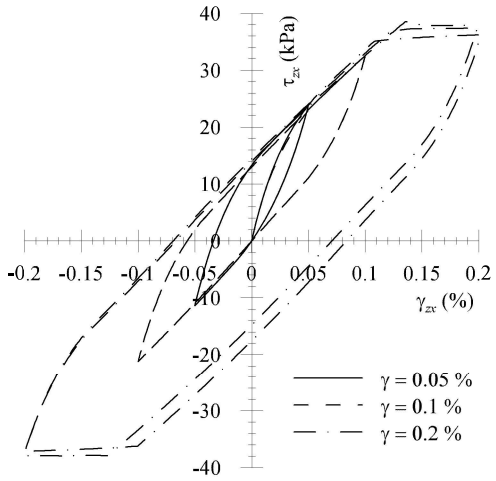

Figure 10
Click here to download Figure: Figure 10.pdf

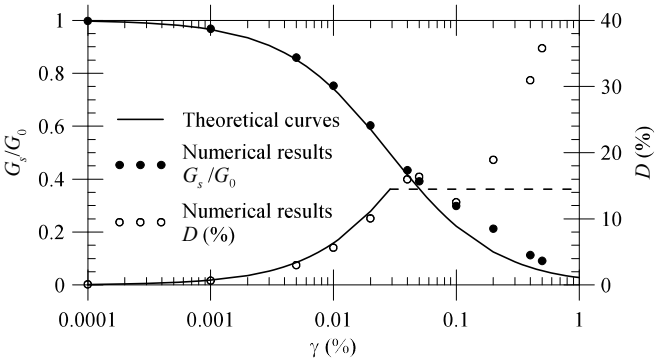

Figure 11
Click here to download Figure: Figure 11.pdf

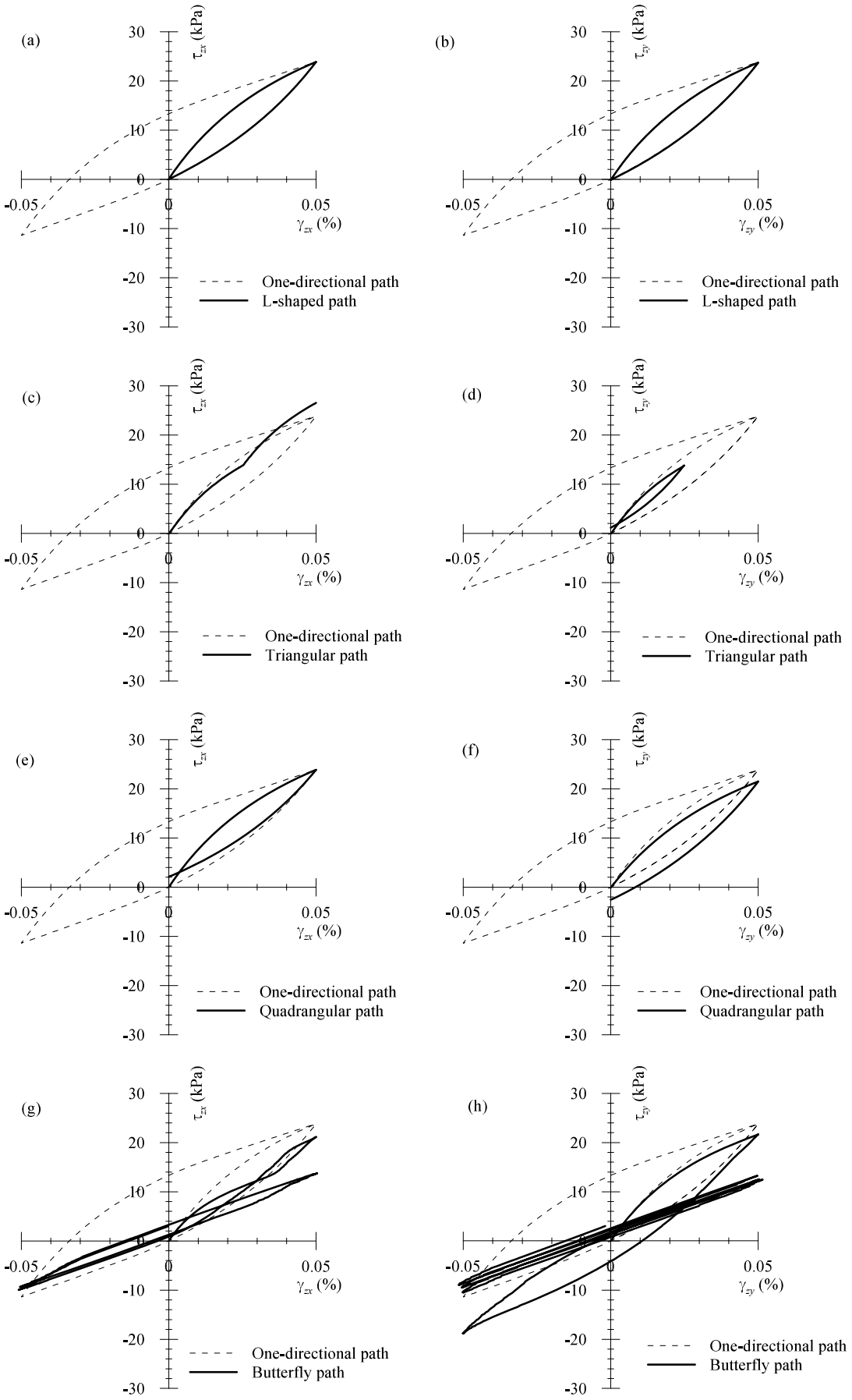

Figure 12
Click here to download Figure: Figure 12.pdf

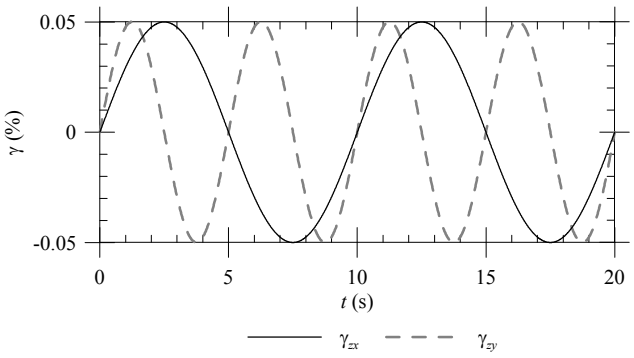

Figure 13
Click here to download Figure: Figure 13.pdf

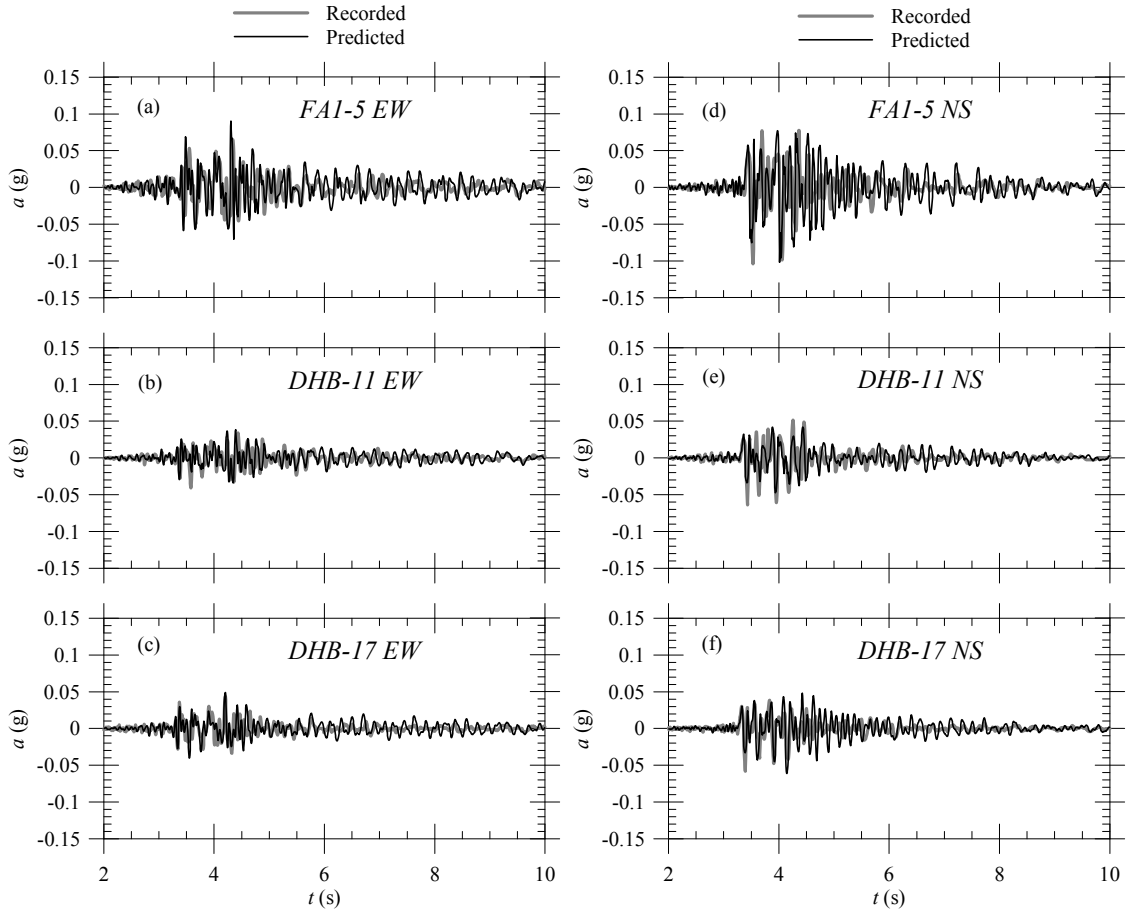

Figure 14
Click here to download Figure: Figure 14.pdf

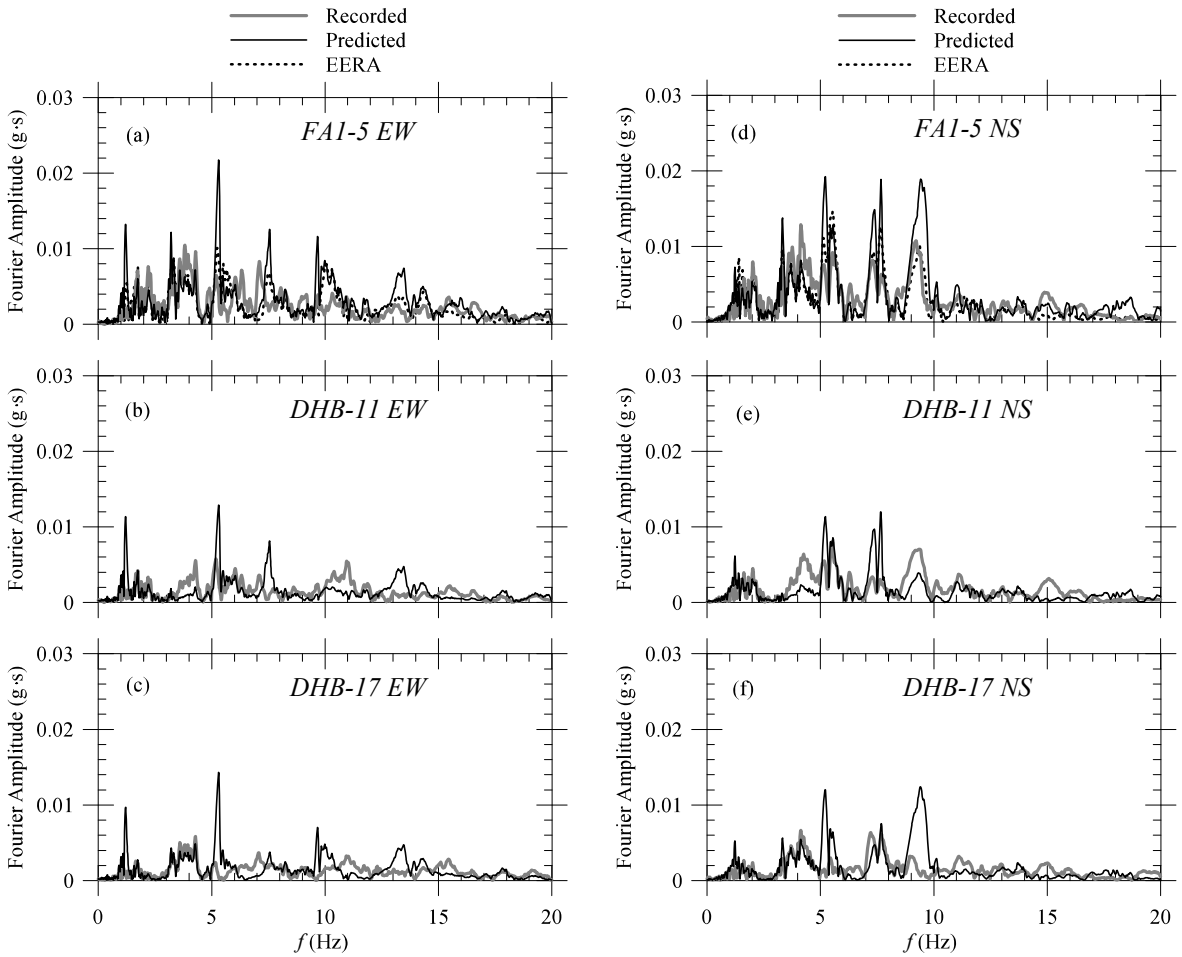

Figure 15
Click here to download Figure: Figure 15.pdf

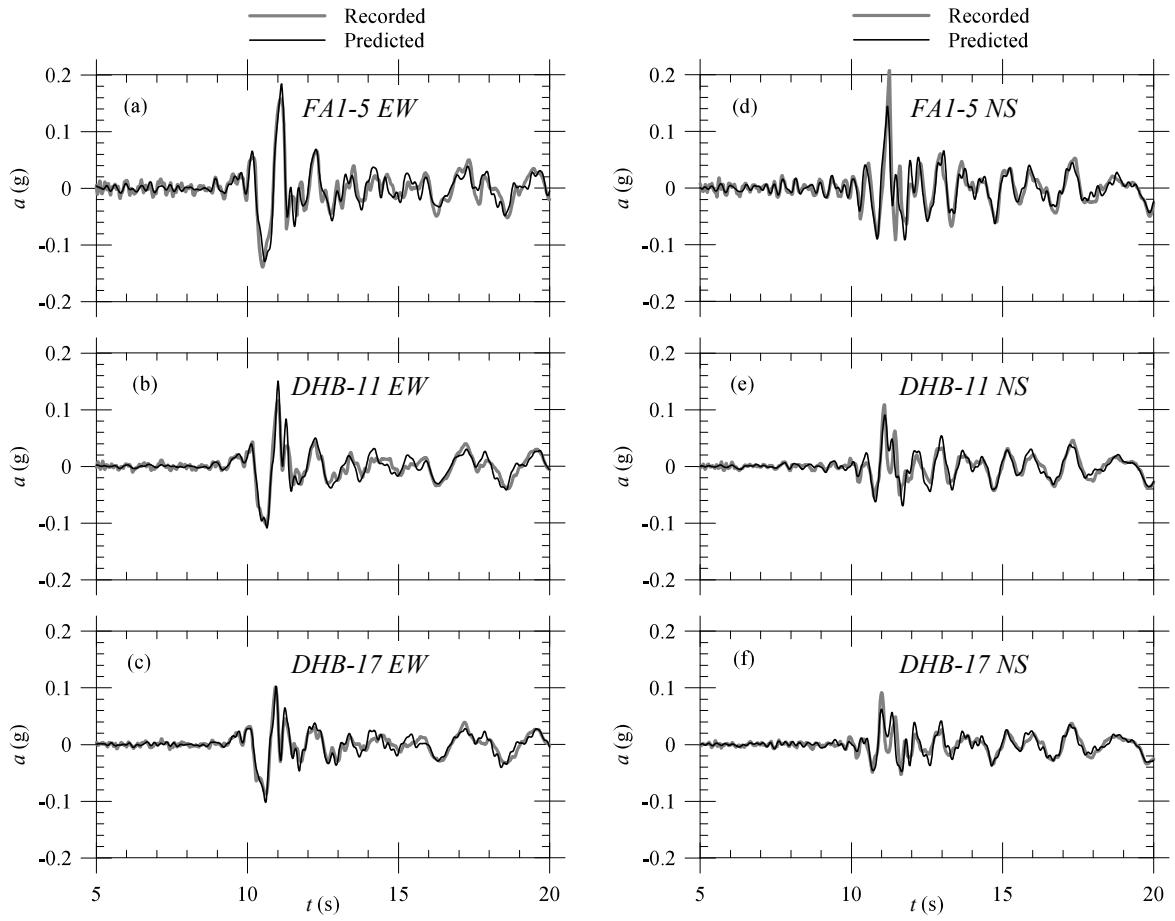

Figure 16
Click here to download Figure: Figure 16.pdf

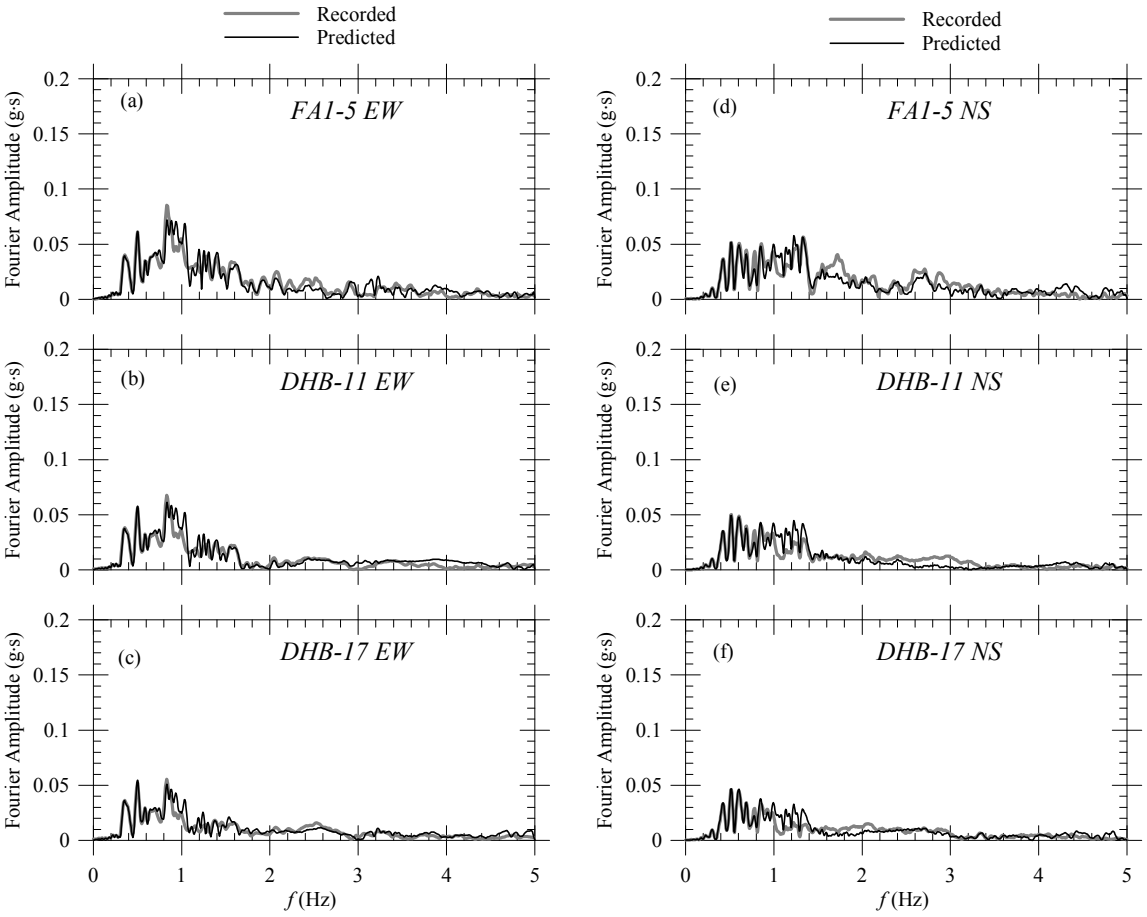

Figure 17
Click here to download Figure: Figure 17.pdf

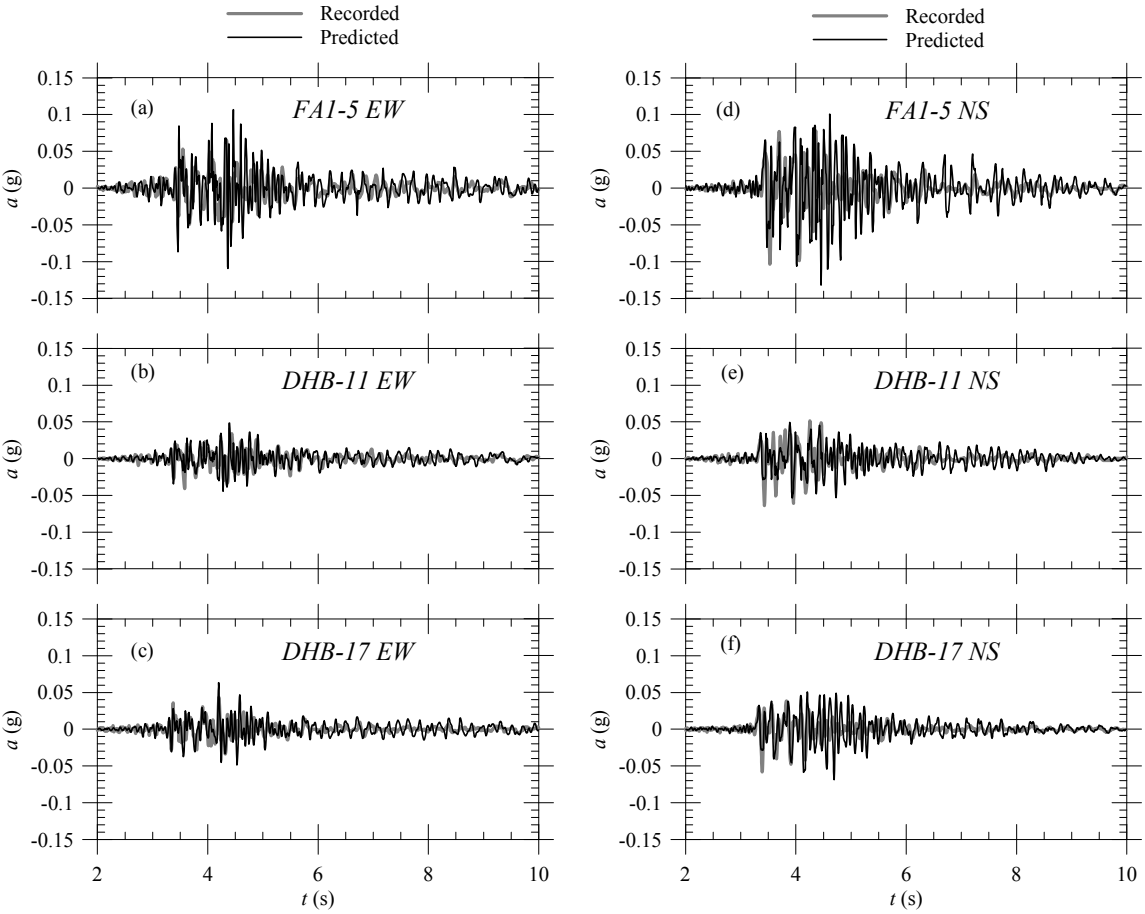

Figure 18
Click here to download Figure: Figure 18.pdf

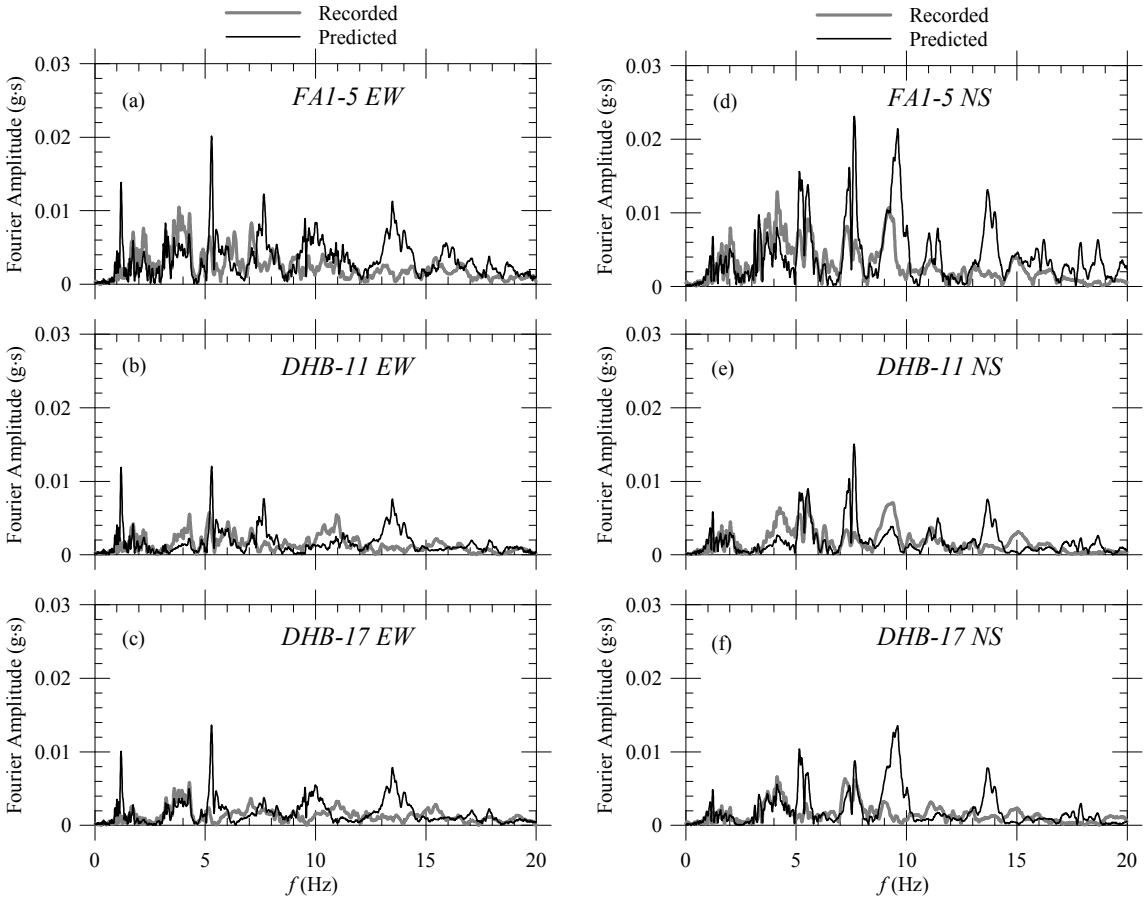

Figure 19
Click here to download Figure: Figure 19.pdf

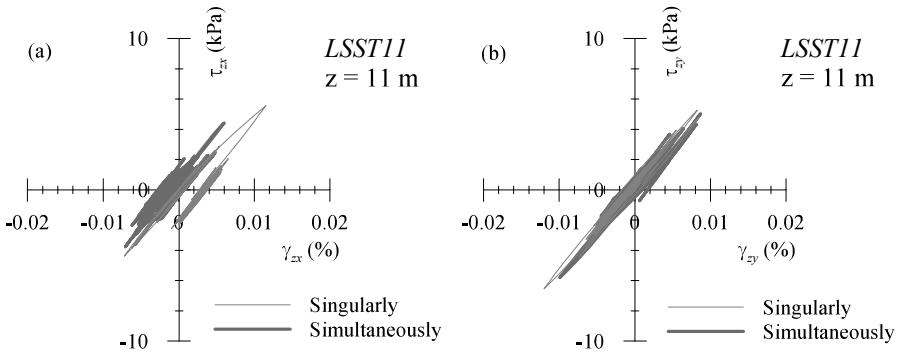

Figure 20
Click here to download Figure: Figure 20.pdf

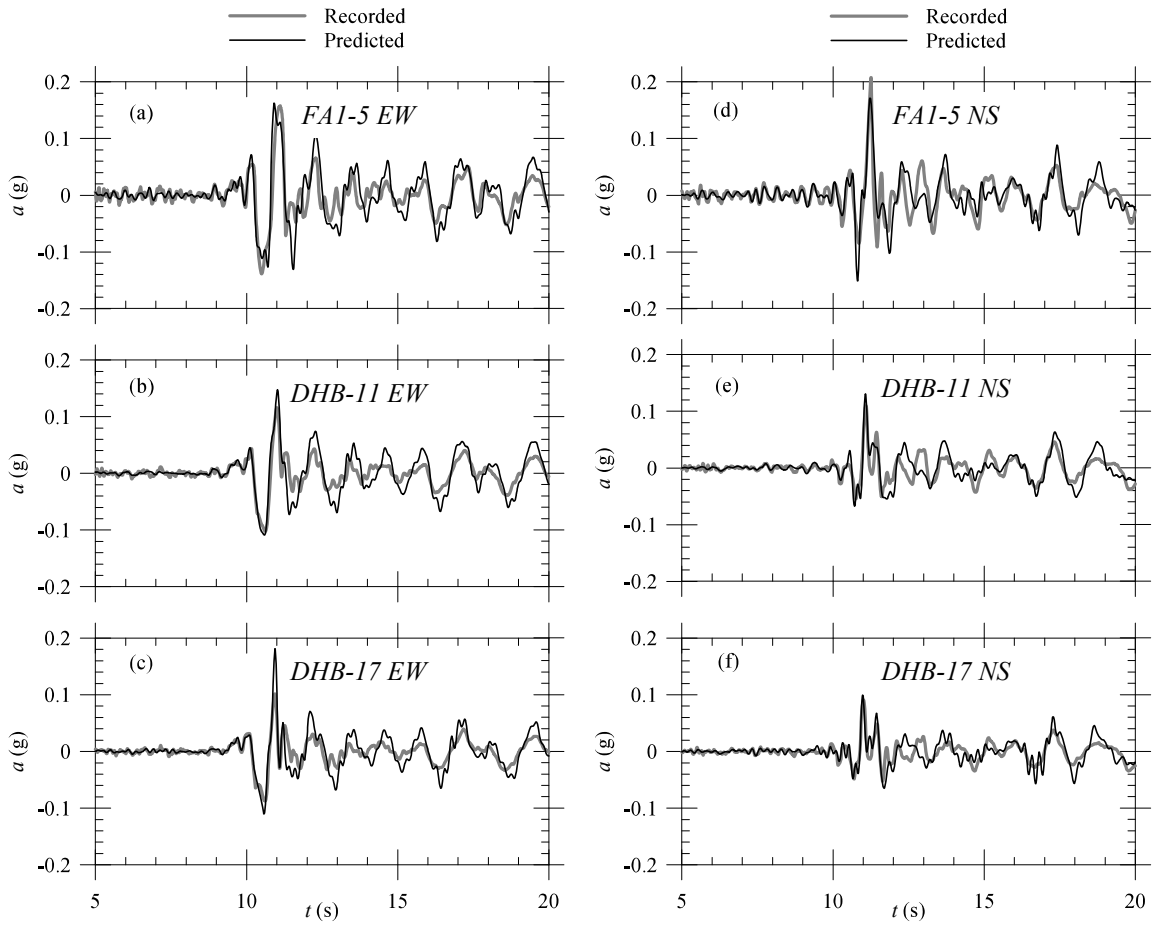

Figure 21
Click here to download Figure: Figure 21.pdf

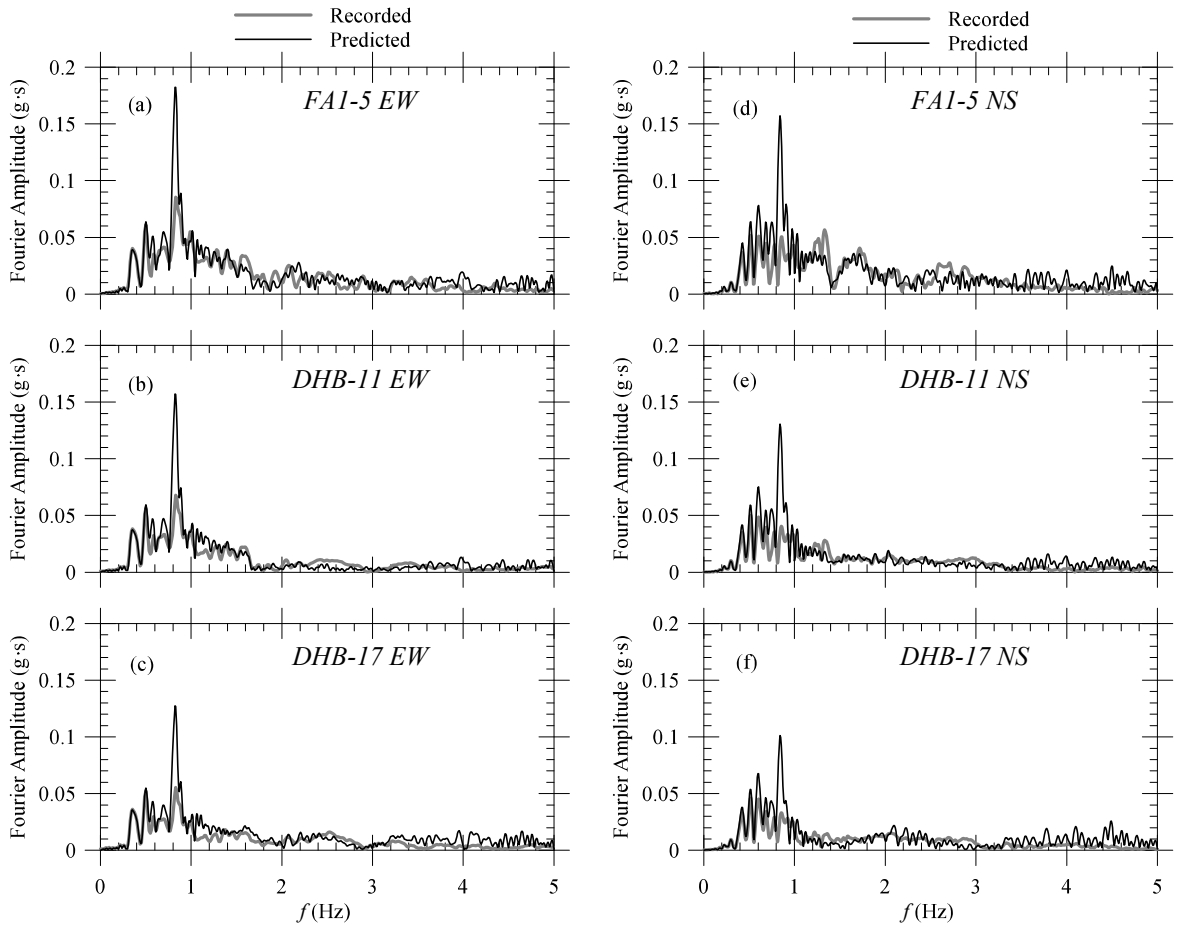

Figure 22
Click here to download Figure: Figure 22.pdf

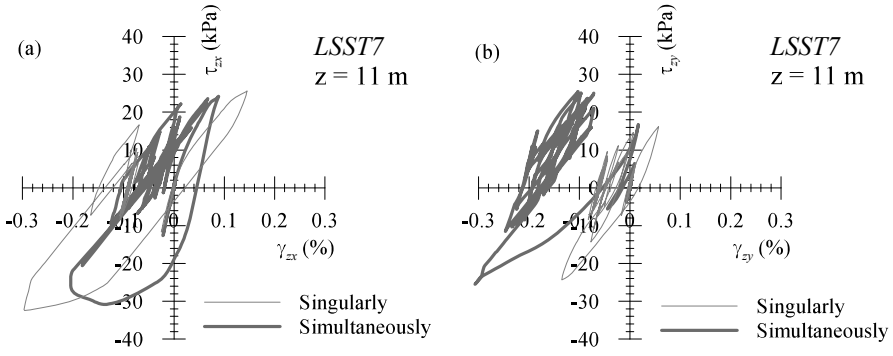

Figure 23
Click here to download Figure: Figure 23.pdf